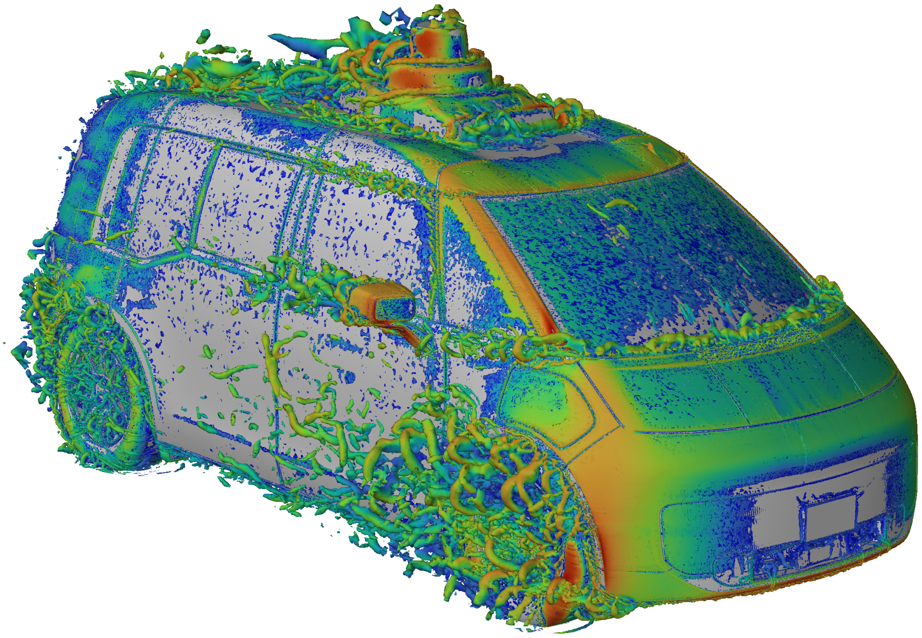

Development of an Aeroacoustic Simulation Procedure for Passenger Vehicles

An investigation on autonomous vehicle wind noise.

Master's thesis in Mobility Engineering

CARL NARUP
NITISH PALANNA

DEPARTMENT OF MECHANICS AND MARITIME SCIENCES
CHALMERS UNIVERSITY OF TECHNOLOGY
Gothenburg, Sweden 2024
www.chalmers.se

Master's thesis 2024

Development of an Aeroacoustic Simulation Procedure for Passenger Vehicles

An investigation on autonomous vehicle wind noise.

CARL NARUP
NITISH PALANNA

Department of Mechanics and Maritime Sciences
Vehicle Engineering and Autonomous Systems
Chalmers University of Technology
Gothenburg, Sweden 2024

Development of an Aeroacoustic Simulation Procedure for Passenger Vehicles
An investigation on autonomous vehicle wind noise.
CARL NARUP
NITISH PALANNA

Supervisor: Adam Brandt, Energy Dynamics, Zeekr Technology Europe
Examiner: Simone Sebben, VEAS, Chalmers University of Technology

Master's Thesis 2024
Department of Mechanics and Maritime Sciences
Chalmers University of Technology
SE-412 96 Gothenburg
Telephone +46 31 772 1000

Cover: Velocity magnitude ranging from 0 m/s to 70 m/s plotted on an iso surface of Q-Criterion of $2 \cdot 10^5$.

Typeset in LaTeX
Printed by Chalmers Reproservice
Gothenburg, Sweden 2024

Development of an aeroacoustic simulation procedure for passenger vehicles
CARL NARUP
NITISH PALANNA
Department of Mechanics and Maritime Sciences
Chalmers University of Technology

Abstract

With the shift to electric powertrains, wind noise has become a proportionally larger contributor to the overall noise levels inside the vehicle. Considering the correlation between noise and premium brand quality and the demand by the customers for quieter vehicles, manufacturers are spending more resources determining noise contribution and ways to quantify, understand and dampen sources of wind noise. The cost of performing aeroacoustic wind tunnel experiments is high. Therefore, methods to predict wind noise using aeroacoustic computational fluid dynamics (CFD) simulations can establish a correlation between wind noise outside and inside the cabin at an earlier stage in the product development.

Experimental data was obtained from accelerometers placed on the left-hand side driver's window and the quarter glass window. An aeroacoustic CFD simulation method was developed and a correlation was obtained with the experimental data. The pressure fluctuations were simulated using unsteady scale resolving flow simulations, with the data being stored as a time series data. A fast fourier transform (FFT) was implemented to decompose the pressure data into its constituent frequency spectrum. Both simulation and experimental data were analyzed using third octave analysis to determine the sound pressure level (SPL) for discretized octave bands. Studies for the mesh size and the time step were carried out to ensure the pressure waves are sampled adequately spatially and in time. Comparisons were made by means of a delta analysis between baseline and modified configurations with results showing that the simulation was accurate in predicting SPL delta values and trends for most configurations.

The simulation method was implemented on a range of geometry changes pertaining to the placement of the advanced driver assistance systems (ADAS) to evaluate the change in the noise levels on the external body due to the addition of driver assistance systems.

Keywords: Aeroacoustics, Computational Fluid Dynamics (CFD), Computational Aeroacoustics (CAA), Advanced Driver Assistance Systems (ADAS), Fast Fourier Transform (FFT), Autonomous Vehicles.

Acknowledgements

We would firstly like to extend our many thanks our colleagues at Zeekr Tech Europe for allowing us to complete our master thesis at the company. A special thank you to our supervisor, Dr. Adam Brandt for his unwavering support and invaluable insight. His willingness to always go the extra mile to help us out is greatly acknowledged.

Our gratitude goes out to Dr. Jesper Marklund, Charlotte Eisner, and Mark Saukkonen for hand picking us to carry out this thesis. We are honored and humbled to have this opportunity to develop Aeroacoustic simulation methods for Zeekr Tech Europe.

Our thanks also goes out to the other master thesis students at Zeekr Tech Europe. It was great to have someone beside us that was going through the same struggles and to play ping-pong with.

Furthermore we would like to extend our many thanks to our examiner at Chalmers University of Technology, Prof. Simone Sebben, for providing valuable feedback and insight into our project scope and direction and for taking her valuable time to be the examiner of our thesis.

Finally a special thank you to Mr. Vijay Palanna and Mrs Vinaya Palanna, as well as Mr. Micael Narup and Mrs. Ewa Narup, without whose unconditional support this project would have never been possible.

Carl Narup, Nitish Palanna, Gothenburg, May, 2024

List of Acronyms

Below is the list of acronyms that have been used throughout this thesis listed in alphabetical order:

ADAS	Advanced Driver-Assistance Systems
CAA	Computational Aeroacoustics
CFL	Courant–Friedrichs–Lewy
FFT	Fast Fourier Transform
FWH	Ffowcs Williams-Hawkings
HVAC	Heating Ventilation and Cooling
LHS	Left Hand Side
LIDAR	Light detection and ranging
NRBC	Non Reflecting Boundary Conditions
OASPL	Overall Sound Pressure Level
ORVM	Outside Rear View Mirror
PID	Part Identification
RADAR	Radio detection and ranging
RMS	Root Mean Square
ROI	Region of Interest
SBES	Stress Blended Eddy Simulation
SPL	Sound Pressure Level
SRS	Scale Resolving Simulation

Nomenclature

Below is the nomenclature of parameters and variables that have been used throughout this thesis.

Parameters

a_{acc}	Measured Accelerometer Acceleration (m/s^2)
a_0	Reference Acceleration corresponding to 1 μ m/s^2
Δk	Resolved-scale turbulent kinetic energy
F_S	Sampled Frequency
F_R	Max resolved Frequency
$\overline{P}$	Mean Pressure
P_{ref}	Reference Pressure corresponding to 20 μPa
P'	Instantaneous Pressure
P'_{rms}	RMS of the Instantaneous Pressure
V_{veh}	Vehicle Velocity
V_{res}	Resultant Velocity
V_{sw}	Side Wind Velocity

Variables

ψ	Yaw Angle
Δ	Delta

Contents

1

Introduction

Wind noise generated by turbulent flows is an increasingly larger dilemma aerodynamics departments are facing when designing battery electric vehicles (BEVs). A paradigm shift in the automotive industry with regards to the shift in development from the internal combustion engines (ICEs) to modern day BEVs, wind noise takes over as one of the main contributors to sound carried into the cabin, predominantly at speeds greater than 100 kmph [1].

Demands on passenger vehicles are becoming evermore stringent encouraging automakers to plan for the future of the automobile industry. By 2026 European regulations will lower the current sound limit emitted by passenger vehicles from today's limit of 72 dB to 68 dB, which is still higher than the 55 dB limit proposed by the WHO [2]. These laws are pioneering vehicle optimization, highlighting the importance of acoustics when designing vehicle geometries.

1.1 Background

The Zeekr M-Vision Concept is Zeekr's autonomous driving platform in collaboration with Waymo, an autonomous technology based in California, USA, which utilizes an ADAS system placed on the roof of the vehicle.

Figure 1.1: Zeekr M-Vision Concept

These geometries are instances where highly turbulent flow may occour, if not designed with careful consideration. A common practice to reduce turbulent wake may include rounding out the a-pillar or optimising the side-view mirror. Turbulent flow near the external body of the vehicle has a substantial effect on the comfort level of the passengers as the sound propagates into the vehicle through green-house panels and other body panels. Prominent during long periods of highway driving, noise caused by sound transmission into the cabin via the green house panels can prove to be fatiguing for the drivers and passengers [3]. Hence, a need for early aeroacoustic geometry changes has become pivotal for vehicle performance and a reliable method to predict the wind noise levels have become imperative. One of these tools is aeroacoustic simulations, which enable early-phase development and improvement of vehicle geometry with regards to wind noise.

Since its introduction, computational fluid dynamics (CFD) has become a vital aspect in the transportation engineering solutions. CFD has been instrumental for the creation of more efficient vehicle geometry and currently plays a vital role in the advancement of many aerodynamics departments in industry. For instance, various design ideas can be investigated early on in the product development phase with a better understanding of the flow regime, giving the ability to produce optimized solutions for a lower cost than using traditional wind tunnel tests.

Methods can be implemented to analyze the aeroacoustic behavior of the vehicle using CFD software. Computational Aeroacoustics (CAA) can be implemented in order to observe the aeroacoustics of the flow around the vehicle as it allows for a comprehensive prediction of realistic aeroacoustic behavior with a wide range of post-processing abilities. [4]

1.2 Purpose

The purpose of this thesis is to develop an aeroacousitc CFD simulation procedure using Ansys Fluent that can be used to analyze sound sources and improve vehicle build quality.

This Thesis aims to develop and validate numerical methodologies to quantify the aerodynamic noise that emanates from current day autonomous hardware and driver assistance systems in BEVs such as LIDARs (Light detection and ranging) and RADARs (Radio detection and ranging). Based on the data obtained from a previously held wind tunnel test, the goal is to obtain a robust and reliable simulation data that can provide results that best correlate with the wind tunnel data and can be implemented for a whole range of Aeroacoustic simulations. The region of interest (ROI) for this study is primarily focused on the the left hand side a-pillar, side mirror, quarter glass and the front side window.

The aeroacoustics of the ADAS will also be investigated using the developed CFD method. The geometry will be shifted and the change in measured SPL will be observed.

1.3 Limitations

Below is a list of a few factors affecting the results and scope of this thesis. A few overarching themes include time, scope and resources

- Students are given 20 weeks to complete the master thesis followed by a report and presentation.
- The geometry of the vehicle had to be simplified with a closed underhood and a flat underbody floor in order to minimize simulation time.
- This method only correlates sound propagation through green-house panels. A model to propagate the sound through the roof and other surfaces was not modelled.
- The time step had to be limited to meet feasible simulation times, which limits the upper frequency range of the numerical results to 3150 Hz. Effects above cannot be captured by the numerical analysis.
- The experimental results were collected in a wind tunnel not adapted for aeroacoustic measurements.
- Experimental results did not include a configuration with the autonomous geometry such as LIDAR or RADAR geometries, limiting the comparability for the simulations with the LIDAR and RADAR hardware.

2

Theory

The following section describes the fundamental theory used to support this thesis. The theory pertains to both numerical and experimental data collected to produce reliable and informed conclusions. Fluid dynamics, aeroacoustics and CFD theory will be presented.

2.1 Aeroacoustics

Aeroacoustics is the study of sound generated from fluid motion and explores strategies for how aerodynamic systems can be designed to reduce noise. [5] This thesis will focus on the sound emitted due to the solid surface interaction with the wind, including the whole vehicle body as a sound source. The predominent areas of interest include the a-pillar, the side-view mirror and other protruding sections of the vehicle such as the LIDAR and RADAR geometries.

2.1.1 Sound

Sound is defined as pressure fluctuations that propagate as a fusion of various frequencies in an elastic medium [6]. Sound can be represented as a superposition of pressure waves of various amplitudes (A) and frequencies (f). For a visual representation, see figure 2.1.

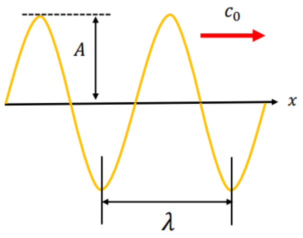

Figure 2.1: Amplitude (A), wavelength (λ), and the speed of sound (c_o). [7]

Frequency is defined as the number of oscillations per unit of time completed by a pressure wave. It may also be defined by the speed of sound and the wavelength of the oscillation as seen in equation 2.1. Frequency is measured in Hz [SI=$\frac{1}{s}$]. Humans can detect sounds from 20 Hz to 20,000 Hz. Low pitch sounds are audible from 100Hz and higher pitch sounds are audible above 1000 Hz.

$$f = \frac{c_0}{\lambda} \tag{2.1}$$

The pressure that facilitates sound is crucial to defining the sound pressure level (SPL) and is measured in decibels [dB]. Human audible sound pressure levels range from 20μPa to 20 Pa resulting in a 1:10,000,000 scale difference. Such scale size is impractical, hence why a logarithmic decibel scale is applied. Sound pressure level is the logarithmic translation of audible pressure fluctuations and is defined in equation 2.2:

$$SPL = 20 \log_{10} \left(\frac{P'_{RMS}}{P_{\mathrm{ref}}} \right) \tag{2.2}$$

Where:

- P'_{RMS} is the root mean square of the measured pressure and
- p_{ref} is the reference pressure (usually 20 μPa for airborne sound) [8].

There are 3 primary sources contributors of aeroacoustic noise, monopoles, dipoles and quadrupoles.

2.1.1.1 Monopole

An acoustic monopole is characterized by its uniform emission of sound in all directions. A prototypical representation of an acoustic monopole is exemplified by a small sphere whose radius undergoes alternating expansion and contraction. Any sound-emitting source whose physical dimensions are considerably smaller than the wavelength of the emitted sound exhibits monopole behavior, manifesting in an equal distribution of sound emission across all directions [9]. An automotive example of a monopole is the sound from HVAC (Heating ventilation and air conditioning) systems, exhaust systems and air leakage into the cabin. For low mach numbers (M<0.3) the monopole is the most prevalent noise source [10]. This can be seen in Equation 2.3, where the Mach number Ma is not raised to a power, as is the case for dipoles and quadrupoles as seen in equations 2.4 and 2.5

$$I_m \approx \frac{\rho * v^4}{Ma} \tag{2.3}$$

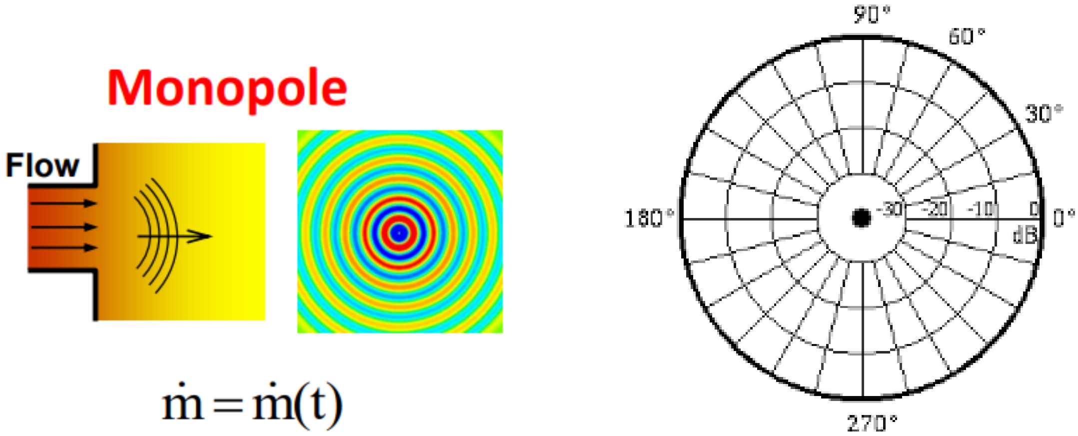

(a) [7] **(b)** [9]

Figure 2.2: Monopoles generate a circular uniform pressure field (a) and the theoretical directivity pattern of a monopole represented as a circleb).

2.1.1.2 Dipole

A dipole source consists of two monopole sources of equal strength but opposite phase and are separated by a small distance compared with the wavelength of the sound. If one source expands the other one contracts resulting in a oscillating movement back and forth between the two sources. The directivity patterns displays a figure eight: two areas where the sound propagates well and two areas of destructive interference.[9] Dipoles are formed due to the interaction of the air with the vehicle body for example regions of separated flows around a side view mirror [10],[11]. Equation 2.4 shows that dipoles are correlated with the cude of the mach number Ma^3, hence it has a relatively lower impact on sound at subsonic flow velocities compared to monopoles.

$$I_d \approx \frac{\rho * v^6}{Ma^3} \tag{2.4}$$

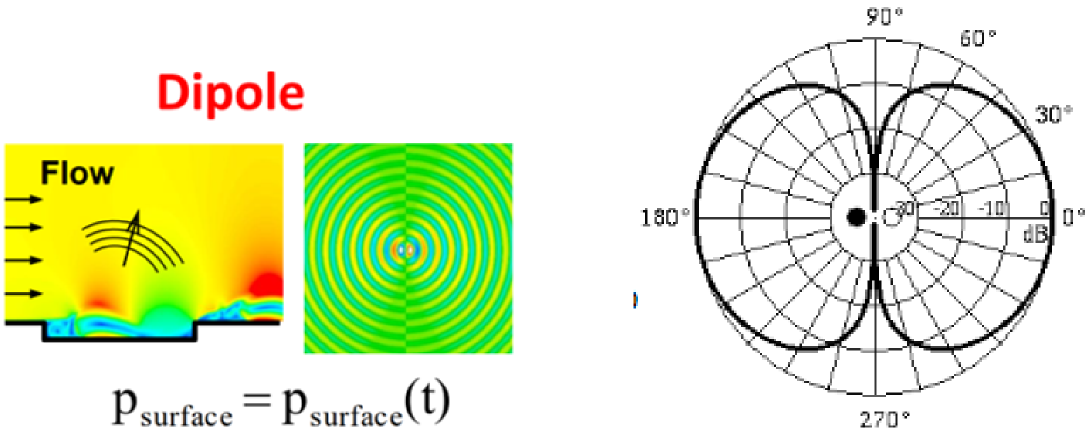

(a) [7]

(b) [9]

Figure 2.3: Dipoles generate an out-of-phase pressure field (a) and the theoretical directivity pattern of a dipole represented by a figure eight (b).

2.1.1.3 Quadrupole

Similar to how two out-of-phase monopoles form a dipole, two out-of-phase dipoles constitute a quadrupole. Quadrupoles arise from collisions of fluid elements and are characteristic of turbulent shear layers found in the wake or mirror of a vehicle [10]. The sound power of monopoles present the most prominent noise source at radiating low frequency which varies at ω^2, followed by dipoles at ω^4 and quadrupoles which at ω^6 [9]. Figure 2.5 illustrates that dipoles are correlated with Ma^5, explaining why quadrupoles are the least prevalent noise sources in automotive applications, while quadrupoles can be the most prevalent noise source in supersonic flows.

$$I_q \approx \frac{\rho * v^8}{Ma^5} \tag{2.5}$$

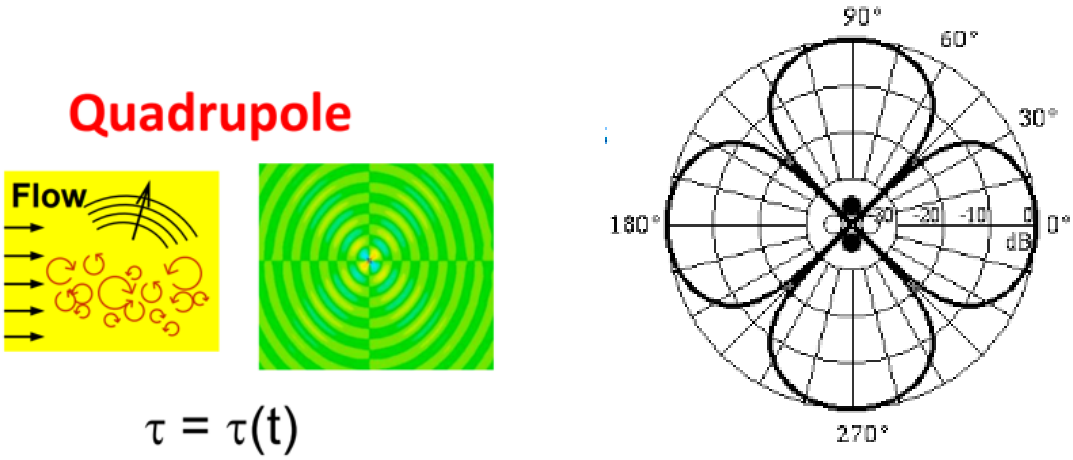

(a) [7] , (b) [9]

Figure 2.4: Quadrupoles generate two out-of-phase dipole pressure fields (a) and the theoretical directivity pattern of a quadrupole represented by a four leaf clover (b).

2.1.2 Fast Fourier Transform

Fast Fourier Transform (FFT) is an algorithm used to efficiently calculate the Discrete Fourier Transform (DFT) and its inverse [12]. The FFT algorithm is widely used in areas of applications were frequency content is required, such as signal processing, audio processing and data compression. The equation used to compute FFT and DFT is the same, as shown in equation 2.6

$$X(k) = \sum_{n=0}^{N-1} x(n) e^{-i2\pi \frac{kn}{N}} \tag{2.6}$$

The DFT transforms a sequence of N complex numbers into another sequence of N complex numbers, representing the amplitudes and phases of sinusoidal functions at discrete frequencies. Yet, the direct computation of the DFT according to its definition requires O(N^2) operations, posing computational challenges for large inputs.

The FFT algorithm significantly lowers the computational complexity of the DFT to O(N log N), greatly accelerating processing for large inputs. This improvement is accomplished by leveraging the symmetry properties of complex exponentials and recursively breaking down the DFT computation into smaller sub-problems.

The FFT can be used to analyze the frequency of sound and compare it to the SPL at each reciever location on the left hand side quarter glass and side window on the vehicle.

2.1.2.1 Third Octave Analysis

Third octave analysis ($\frac{1}{3}$ octave analysis) is a method of grouping sound frequencies across specific frequency bands corresponding to one-third of an octave [13]. This division allows for a more detailed octave analysis, as each band that spans one octave is split into three, meaning one band has less incorporated frequencies and more fluctuation is observed. For instance, the 16Hz band in standard octave analysis would be broken into 12.5Hz, 16Hz and 20Hz for one-third octave analysis.

Each Band has a standardized center frequency f_0 accompanied by a lower and a higher limit that defines the frequency band. The higher and lower limit can be calculated using equations 2.7 and 2.8 as shown [14]:

$$f_{low} = \frac{f_0}{\sqrt{2}^{\frac{1}{3}}} \tag{2.7}$$

$$f_{high} = f_0 \cdot \sqrt{2}^{\frac{1}{3}} \tag{2.8}$$

2.2 Computational Fluid Dynamics

Fluid dynamics encompasses the motion of fluids [15]. This section will give detailed accounts of the physical supporting theories and equations used in CFD. The turbulence modeling is broken into its constituents, focusing on Reynolds-Averaged Navier-Stokes (RANS), Large Eddy Simulation (LES), and Stress-Blended Eddy Simulation (SBES).

2.2.1 Turbulence Modeling

Turbulence dominates the flow surrounding a vehicle. From the turbulent boundary layer found on the hood to the turbulent wake caused by side-view mirror. Turbulent flows present a multi-scale challenge. Big structures in the atmosphere can be observed to have a length scale of kilometers down to the smallest kolmogorov scales, where the length scale are measured in micrometers. [16] Resolving all scales is possible with direct numerical simulations, however, it would require a mesh that is fine enough to resolve all turbulent scales, which can be extremely expensive. Alternatively, eddies that are larger than the mesh can be resolved using the LES approach. [17].

Turbulence modeling allows for an understanding of turbulent flow behavior without the cost of expensive turbulent-resolving calculations. Modeling turbulence gives an understanding of flow behavior without resolving the turbulent structures. One common approach is to model all turbulent flow in the fluid in time which results in the Reynolds-Averaged Navier-Stokes (RANS) equation. RANS is a steady-state solution wich is good for a basic understanding of the flow around a geometry. [4]

2.2.1.1 RANS

The Reynolds-averaged Navier-Stokes (RANS) equation systematically decomposes the flow variables into mean and fluctuating components, isolating the mean flow effects from those attributed to turbulent fluctuations.

$$\frac{\partial \overline{\mathbf{u}}}{\partial t} + (\overline{\mathbf{u}} \cdot \nabla)\overline{\mathbf{u}} = -\frac{1}{\rho}\nabla \overline{p} + \nu \nabla^2 \overline{\mathbf{u}} - \frac{\partial \overline{\mathbf{u}'\mathbf{u}'}}{\partial x_j} \tag{2.9}$$

The RANS equation is displayed in equation 2.9. The time averaged variables are represented by a bar ($\overline{p}$) and the instantaneous variables by an apostrophe (u'). In equation 2.9, the mean velocity field ($\overline{\mathbf{u}}$) is influenced by various forces and phenomena. The convective acceleration term describes how the mean velocity changes as it moves through space, reflecting the impact of the mean flow itself. Additionally, the equation considers the effects of pressure gradients, viscosity, and turbulent fluctuations. The pressure gradient ($-\frac{1}{\rho}\nabla \overline{p}$) force arises from pressure variations, while the viscosity term ($\nu \nabla^2 \overline{\mathbf{u}}$) accounts for momentum diffusion due to fluid viscosity. Turbulent fluctuations, represented by the Reynolds stress tensor ($\frac{\partial \overline{\mathbf{u}'\mathbf{u}'}}{\partial x_j}$), contribute to the overall momentum balance by transferring momentum between the mean flow and turbulent fluctuations.

Reynolds-Averaged Navier-Stokes (RANS) simulations provide steady-state solutions by averaging turbulence effects over time. This approach reduces computational demands and facilitates a comprehensive understanding of flow patterns. RANS is particularly effective for analyzing boundary layer flows around smooth structures like vehicle hoods or roofs, where the boundary layer remains attached to the surface. This method is widely employed in complex turbulent simulations involving such configurations, thanks to its ability to capture boundary layer behavior accurately. On the other hand, RANS has trouble predicting flow separation. This is due to the simplification of flow regimes that may not capture complex behavior of turbulence accurately, particularly in adverse pressure gradients and separated flows. RANS often struggles predicting Reynolds stresses near separation points, leading to poor predictions of the onset and extent of sepration. It also deals with time averaged quantities, meaning that no transient behavior are resolved, which drastically affect the ability to predict flow separation.

Due to these reasons, more advanced methods such as Large Eddy Simulation (LES) are often preferred for flows involving significant separation, as they can resolve the turbulence scales more accurately. However, these methods are computationally expensive compared to RANS, which is why RANS is still widely used in engineering practice despite its limitations.

2.2.1.1.1 k-ω Turbulence Model The k-ω turbulence model provides additional closure for the turbulent viscosity in the RANS equations. It is a two equation model, see equation 2.10 and 2.11.

$$\frac{\partial k}{\partial t} + \overline{\mathbf{u}} \cdot \nabla k = P - \beta^* \rho k \omega + \frac{\partial}{\partial x_j}\left[(\nu + \sigma_k \frac{k}{\omega})\frac{\partial k}{\partial x_j}\right] \tag{2.10}$$

$$\frac{\partial \omega}{\partial t} + \overline{\mathbf{u}} \cdot \nabla \omega = \frac{\alpha}{\omega} P - \beta \rho \omega^2 + \frac{\partial}{\partial x_j} \left[(\nu + \sigma_\omega \frac{k}{\omega}) \frac{\partial \omega}{\partial x_j} \right] \tag{2.11}$$

The k-ω model accounts for convection and diffusion of turbulent energy.The model is used for accuracy, robustness, and predictive capabilities. It is well suited for simulating flows near walls where turbulent effects are significant.

2.2.1.2 Large Eddy Simulation

Large Eddy Simulations (LES) is a transient solution that resolves the flow in space. LES resolves large eddies that are larger than the mesh size, while smaller scales are modeled by the sub-grid scale model. In order to model smaller scales, LES applies a filter to average the affects of small eddies to lighten the computational cost. This involves blending the characteristics of small eddies over a particular scale. The filtering equation can be observed in equation 2.12:

$$\overline{u}(\mathbf{x}, t) = \int_{-\infty}^{\infty} \int_{-\infty}^{\infty} \overline{u}(r, \tau) G(\mathbf{x} - \mathbf{r}, \mathbf{t} - \tau) dr d\tau \tag{2.12}$$

where:

- $\overline{u}(\mathbf{x}, t)$ is the filtered field variable.
- $\overline{u}(r, \tau)$ is the unfiltered field variable at position r and t.
- $G(\mathbf{x} - \mathbf{r}, \mathbf{t} - \tau)$ is the filtering kernel applied to the field variable.
- The double integral suggests that the filtering over time and space.

The equation for the modified LES Navier-Stokes equation for incompressible flow is shown below in equation 2.13.

$$\frac{\partial \overline{u}_i}{\partial t} + \overline{u}_j \frac{\partial \overline{u}_i}{\partial x_j} = -\frac{1}{\rho} \frac{\partial \overline{p}}{\partial x_i} + \nu \frac{\partial^2 \overline{u}_i}{\partial x_j \partial x_j} - \frac{\partial \overline{\tau}_{ij}}{\partial x_j} + \overline{f}_i \tag{2.13}$$

where:

- $\overline{u}_i$ represents the filtered velocity,
- $\overline{p}$ represents the filtered pressure,
- $\overline{\tau}_{ij}$ represents the sub-grid scale stress tensor, and
- $\overline{f}_i$ represents any external body forces acting on the fluid.

A commonly used method to model the sub-grid scales is the Wall Adapting Local Eddy Viscosity (WALE) model. The WALE model is used in Large Eddy Simulation (LES) to improve the accuracy of simulations near solid boundaries. The WALE model aims to address shortcomings of traditional eddy viscosity models in predicting turbulence behavior near walls. Unlike eddy viscosity models, the WALE model incorporates a wall-distanced function to adjust the eddy viscosity. This allows for the correct flow to be captured near the wall while allowing larger eddies to dominate the outer flow fields.

2.2.1.3 Hybrid RANS-LES

Hybrid RANS-LES is a method used to solve transient turbulent structures in the free stream and in the wakes using LES while modeling flow close to wall using RANS. A shielding function can be implemented to determine where the simulation should utilize the two types of models.

Stress Blended Eddy Simulation (SBES) is a part of a method known as hybrid RANS-LES which aims to provide more accurate and computationally efficient simulations for turbulent flows. SBES integrates the RANS and LES methodologies into a hybrid framework that efficiently computes fluid dynamics of a simulation. The technique utilizes a stress blending function to modulate the influence of RANS versus LES based on their location within the flow field. This strategic blending facilitates the accurate representation of viscosity-dominated phenomena close to walls without necessitating the dense grid resolution typically required for LES. As the flow moves away from these near-wall, viscosity-dominated regions, SBES seamlessly transitions to LES mode to capture the larger and more dynamic scales of turbulence typically associated with expansive turbulent structures.

2.2.2 Wall y^+

The mesh consists of prism layers near the solid walls as described in table 4.4. In order to accurately predict the flow separation features in the near wall region, the y^+ parameter has to be set. The y^+ is a non dimensional wall distance that is used to determine how close to the wall in the turbulent boundary layer the first layer of the computational mesh is. It provides information about the relative size of the first grid cell near a solid surface compared to the thickness of the viscous sublayer in the boundary layer. The height of the first prism layer determine how close to the wall the physics are simulated.

2.2.3 Computational Aeroacoustics

Computational Aeroacoustics (CAA) numerically resolves flow physics over a range of scales to solve for acoustic properties of the fluid flow. CAA solves for transient, compressible flow-field solutions using a high fidelity CFD model and monitor the unsteady static pressure fluctuations using specified receiver points in the flow field. [7]

CAA has various requirements on the simulation set-up, specifically at the reciever locations and around turbulent structures, in order to capture scale-resolving turbulent flow. Measuring the sound in a turbulent flow follows clear numerical requirements [7]. The transmission zone needs to be resolved with at least 20 grid points per wavelength for the highest frequenices of interest. This may be visualized in equation 2.14 below:

$$MeshSize = \frac{\lambda_{min}}{20} \tag{2.14}$$

Where $\lambda min = \frac{c_0}{f_{max}}$. This ensures a good frequency resolution in the resolved-scale turbulent flow field.

The time-step required to capture an adequate frequency range is governed by Courrant-Friedrichs-Lewy (CFL) number and the Nyquist Criterion. The CFL number in fluid convection is the ratio between propagation distance of a fluid particle for a time step Δt and mesh size Δx and is shown in equation 2.15 [7]:

$$CFL = U \cdot \frac{\Delta t}{\Delta x} \tag{2.15}$$

The acoustic CFL number determines the stability of sound propagation. It imposes stringent requirements on the simulation because a small mesh size is needed to satisfy the acoustic CFL condition. Since waves propagate at the speed of sound, the equation for the acoustic CFL number is:

$$CFL_a = c \cdot \frac{\Delta t}{\Delta x} \tag{2.16}$$

This criteria can be used to achieve an appropriate time step for CAA analysis such that the highest frequencies are resolved properly. The correct order is to first chose the mesh size Δx to capture the smallest frequencies, followed by the time step Δt to ensure the CFL criteria is fulfilled.

The Nyquist criterion suggests a correct choice of sampling rate when periodic signals such as sine waves are being digitized. If the sampling rate is not sufficiently high, a phenomenan known as aliasing occurs. Aliasing is an incorrect digital representations of an acoustic sound wave caused by a low sampling rate and softens and lowers the frequency of a measured wave. Nyquist demonstrated that to avoid aliasing, the sampling rate is required to be twice the frequency, or $r > 2f_{max}$ ([18], [19]). This may also be represented using the simulation time step, as shown in equation 2.17:

$$f_{max} = \frac{1}{2.56 \cdot \Delta t} \tag{2.17}$$

The sampling rate will also determine the maximum resolved frequency. To resolve the desired frequency, a sufficient sampling rate must be used.

3

Literature Review

This literature review synthesizes existing research on the sources and impacts of aeroacoustic noise in vehicles, explores the latest advancements in computational modeling and evaluates the implications of these findings for the design and operation of road vehicles.

3.1 Aeroacoustic Mesh

A research article by Chode et al. [20] titled conducted on the noise characteristics of inclined side-view mirror configurations explores the aerodynamic drag and noise characteristics of a standard squareback vehicle with various inclined side-view mirror configurations using a hybrid computational aeroacoustics (CAA) approach. The side-view mirror inclination of 16 degrees minimizes noise, though further inclination does not significantly reduce noise but affects the drag coefficient. These insights are crucial for designing side-view mirrors to balance noise reduction and aerodynamic efficiency in automotive applications. The study places local mesh refinement zones particularly closer to the forebody, which includes the a-pillar, side window and side-view mirror. Several refinement zones were implemented to create a smooth transition between the fine and coarse mesh size and to resolve turbulence to accurately capture flow.

In a study conducted on the noise prediction at the driver-side green-house panels of passenger vehicles it was also suggested to use a mesh refinement around the region of interest. The study deduced that a hexacore mesh elements with a base size of 2 millimeters be used 200 mm in front of the side-view mirror and 1100 mm behind the mirror. A 200 mm thick refinement zone was also used on the side window, also with a base size of 2 mm. The side window was used to take aeroacoustic measurements. [21]

A study on the wind noise tranmission and filtering through glass conducted by He et al determined that a 2 millimeter refinement zone should be placed close to the region of interest, including side-view mirror and a-pillar, followed by a 4 millimeter refinement zone, as refereed to in current research. [22]

3.2 Aeroacoustic Methodology

Perugini et al. [1] studied the interior noise prediction in aeroacoustic development and presents an efficient hybrid computational process for predicting interior noise in aeroacoustic vehicle development. The methodology combines delayed detached-eddy simulation with a finite element model (FEM). This study utilizes OpenFOAM for computational fluid dynamics and Actran for finite element modeling to examine the Lamborghini Urus cruising at a speed of 140 km/h. The aeroacoustic behavior around the side mirror, particularly for frequencies up to 5 kHz, is analyzed. Numerical simulations are validated against experimental data from the aeroacoustic wind tunnel at the University of Stuttgart. Exterior noise propagation and interior noise transmission through the side window are modeled and compared with measurements from exterior and interior microphones, showing good correlation. The study also investigates critical aeroacoustic sources and vortex structures contributing to wind noise. The comprehensive computational aeroacoustics process demonstrates accuracy and suitability for analyzing the generation and transmission of wind noise into the vehicle cabin. Perugini et al. presents a compelling method of interior noise prediction using a combination of CAA and FEM to capture the vibrations in the side window caused by wind noise.

Chode et al. [20] also suggested that a CAA methods are a used to investigate the numerically complex interactions between the flow and turbulent structures, such as the a-pillar and side-view mirror. The study suggests that the hydrodynamic pressure fluctuations are solved using Reynolds-averaged Navier-Stokes. However, for acoustic predictions it is more accurate to use a hybrid RANS-LES approach that partially resolves turbulent flow in eddie-dominated regions and RANS in areas of small scales where averaging is carried out. It was also suggested that a shielding function be used. The stress blended eddie simulation offers a reasonalbe agreement with the aerodynamic prediction of complex vehicle shapes by allowing for rapid transitions from RANS to LES. This method captures the flow separation accurately while preventing grid-induced separation for highly refined grids. [20]

3.3 Noise Sources

Stridh [21] worked developing a method for performing multidisciplinary optimization for automotive applications and was conducted at Zeekr Tech EU (formerly China Euro Vehicle Technology(CEVT)). This type of optimization may lead to better performance insights in relation to contamination, NVH, aeroacoustics and aerodynamics through targeting noise sources at turbulent structures. The study uses two design parameters: the mirror's position along the car and the angle between the car's side and the mirror's interior. The optimization process involves four main steps. The four-step optimization process involves modifying the geometry, generating the simulation domain and volume mesh, simulating flow and calculating optimization parameters, and adjusting design parameters, all automated by a bash script. The study found that angle of the mirror should be increased slightly to reduce the drag and sound pressure level. The optimal x-position of the mirror was found to be outside the investigated area, however, moving the mirror as far back resulted in a decrease in drag. The position of the side view mirror had a small impact on the aeroacoustics at the side window.

4

Numerical Method

The following section describes the numerical methodology used in this project, especially pertaining to the development of the Quasi CAA methodology. The key aspects of the project were design, simulation and post processing. The geometry preparation was carried out using CATIA, Autodesk Fusion 360 and ANSA. The meshing was handled by Fluent meshing in conjunction to the simulation software Fluent solver. The post processing and acoustics analysis of the data was performed in MATLAB.

4.1 Aeroacousitc Simulation Overview

A typical aeroacoustic simulation setup consists of 4 primary stages, the preprocessing stage, simulation stage, postprocessing stage and the validation stage. A more detailed diagram is seen below 4.1.

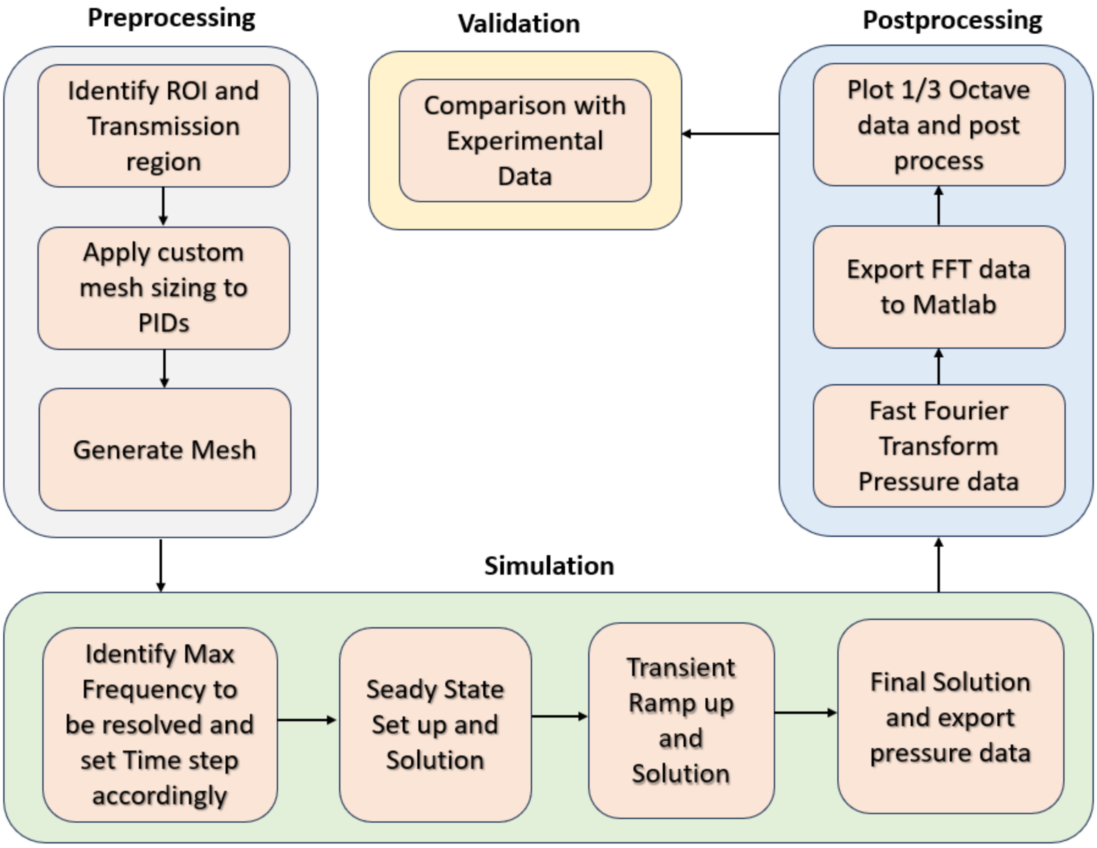

Figure 4.1: A Typical workflow for an Aeroacoustics Simulation

4.2 Computational Model

The test object used for this study was a simplified model of the Zeekr M-Vision concept. The model was simplified by sealing the front intake and implementing a flat underbody as seen in figure 4.2b. The test object is 4.693 m in length, 2.280 m in width including the side view mirrors and 1.800 m in height with a wheelbase of 2.999 m and a track width of 1.700 m.

The model is placed within a right-hand coordinate system. The positive X-direction aligns with the length of the car, extending from the front to the rear. The positive Y-direction lies along the width of the car pointing towards its right side. The positive Z-direction aligns with the height of the vehicle, orienting upwards.

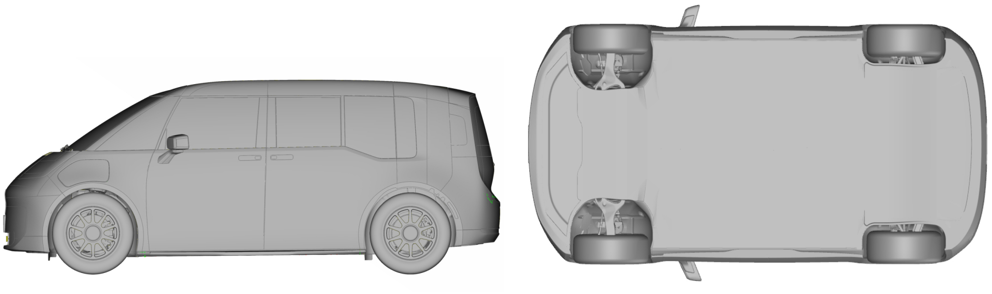

(a) Side view of the Zeekr M-Vision **(b)** Underbody of the Zeekr M-Vision.

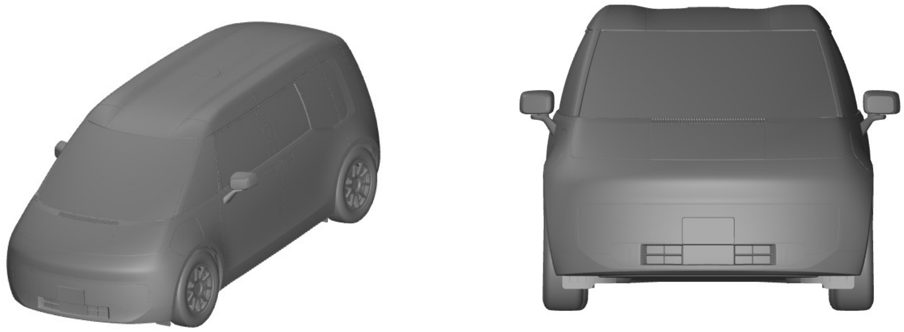

(c) Isometric view of the Zeekr M-Vision **(d)** Front view of the Zeekr M-Vision

Figure 4.2: Computational Model

4.3 Pre-processing

The preliminary step is to identify the region of interest (ROI) for the meshing process, which for preliminary studies was the left side quarterglass and the left hand side front window. 8 monitoring points are defined on the vehicle body, see figure 4.3. This was primarily due to the fact that wind tunnel data was available for this section and hence allowed for a correlation to be made to experimental data. The general methodology can be applied for aeroacoustic analysis for any region of the vehicle. However as evidenced by prior research, the primary contributor for the noise perceived by the passengers is due to the pressure fluctuations in the side windows [23]. For subsequent comparisons with the ADAS systems, no refinement region was used due to the lack of computational resources and time.

The geometry is pre processed and cleaned using the preprocessing software ANSA. The primary objective of using this tool is to close panel gaps and seams that would otherwise cause a mesh with poor quality or would lead to a number of unnecessary volume cells being created either in the underhood or the cabin. Each constituent object in the geometry and the domain is assigned a unique part identity (PID) and label, which can be used to assign custom mesh size functions and refinements in the meshing software.

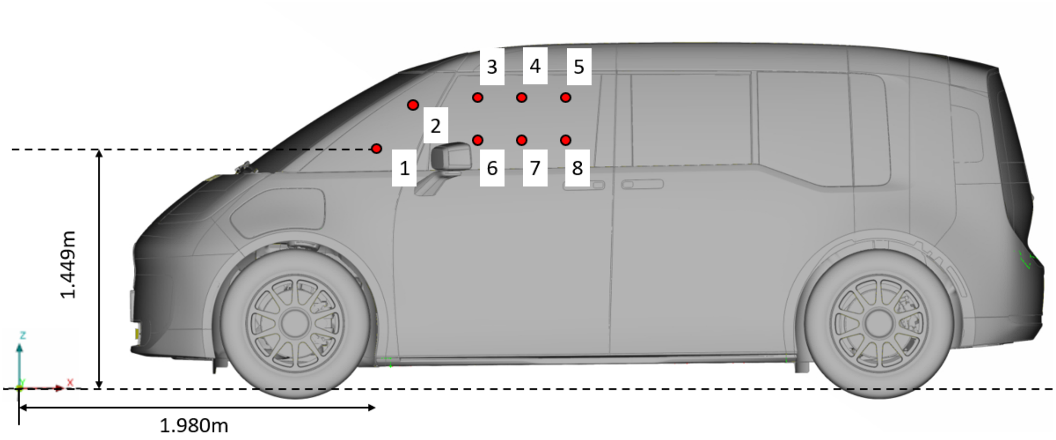

Figure 4.3: Monitoring points in reference to the coordinate system

4.4 CFD Simulation Setup

The following section describes in detail the setup process of the CFD simulation files.

4.4.1 Preliminary Research

4.4.1.1 Wind Tunnel Testing

The team at Zeekr performed an aeroacoustic wind tunnel test of the test model at the Volvo Wind Tunnel PVT prior to the start of the thesis. The test performed includes yaw changes, folding mirrors, changing wiper position and modifing the A-Pillars were performed to evaluate the effect of the wind induced vibrations on the side window and quarter glass that corresponds to the SPL (see equation 4.1)

Although the PVT has proven to produce reliable aerodynamic results in the past, there is a significant amount of self-noisiness produced by the setup. Primarily due to the large fan and the lack of acoustic treatment on the walls [24]. Hence the magnitude of the noise generated in the physical test is significantly louder than what was observed in the simulations.

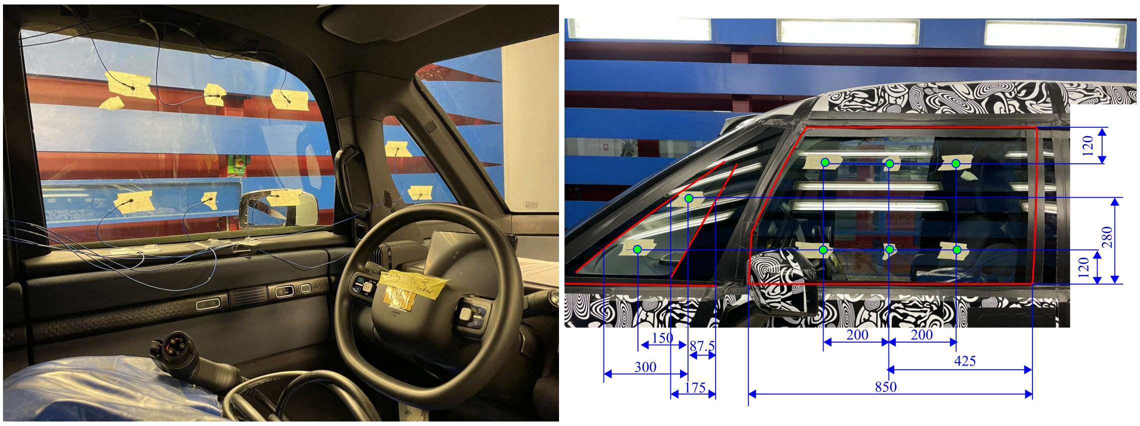

(a) Cabin View of the accelerometers **(b)** Accelerometer positioning

Figure 4.4: Wind tunnel testing of the test object

The SPL readings were taken using 8 accelerometers taped on the inside of the window as seen in 4.15. The accelerometer measures the vibrations in m/s^2 at each point. Using this data, a corresponding SPL in dB can be extracted using the formula in equation 4.1

$$OASPL(dB) = 20log_{10}(\frac{a_{acc}}{a_0}) \tag{4.1}$$

Where a_{acc} is the measured acceleration from the accelerometer in m/s^2 and a_0 is the reference acceleration corresponding to 1 $\mu m/s^2$ [8].

4.4.1.2 Method Development

During the initial phase of the study, multiple approaches for simulating for aeroacoustics were investigated, primarily the CAA (Computational Aeroacoustics) Method, FWH (Ffowcs-Williams Hawkings) Method and the Quasi CAA method which was developed for the purpose of this study.

As mentioned in section 2.2.2, CAA is the process of simulating transient, compressible flow fields and monitoring the unsteady static pressure fluctuations at predetermined locations in the domain [25]. Traditionally CAA is computationally intensive due to density changes being simulated and the fine mesh requirement.

The FWH method implements an acoustic model that is used to predict the sound propagation in the transmission region. This reduces the simulation time however this model has several key limitations such as not accounting for the reflection and scattering of sound outside the source region and in general this method is not applicable for cases where the sound needs to be analysed in regions close to walls. Both the CAA and FWH methods require specific non reflecting boundary conditions (NRBCs) which require an acoustic CFL number of 1 (see equation 2.16. This metric was observed to be a challenge to meet since it requires an extremely low time step as seen in equation 2.16.

The Quasi CAA method combines key attributes with regards to the CAA method such as resolving sound using the Naiver Stokes equations and integrates it with an aerodynamic mesh. The static pressure changes are recorded by using predetermined points in the domain. User defined functions as seen in equation 4.6 and equation 4.9 are implemented to obtain the field function for the sound intensity and the RMS of pressure respectively.

Table 4.1: Primary differences between the CAA, FWH and Quasi CAA

	CAA	**FWH**	**Quasi CAA**
Energy	On	Off	Off
Density	Ideal Gas	Constant	Constant
Pressure fluctuations	Simulated	Modeled	Simulated
Density fluctuations	Simulated	Modeled	Ignored
Sources	All flow	Vehicle external walls	All flow
Receivers	No	Yes	No
Wall Treatment	Sponge Layers/NRBC	Sponge Layers/NRBC	None
Computational Cost	High	Moderate	Moderate

4.4.2 Computational Domain

The domain is 80 m long, 20 m wide and 14.815 m high.

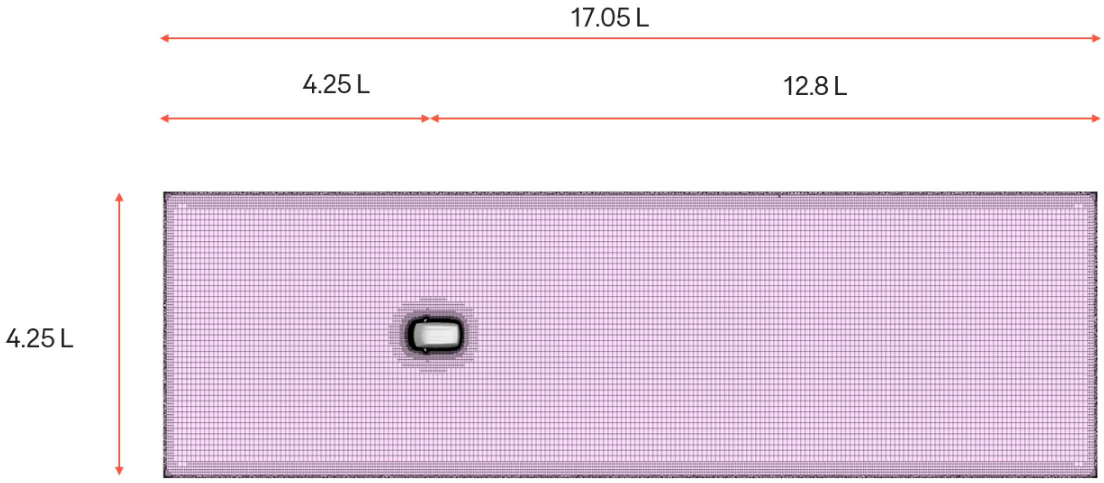

Figure 4.5: Computational Domain

4.4.3 Simulation Parameters

The inlet velocity was set to be 130 km/h, as were the conditions for the wind tunnel test. The domain consists of one inlet at the -X boundary and one outlet at the +X boundary. The ground is set to a stationary wall boundary condition while the side boundaries and the roof are set to a symmetry boundary condition. The objective of this is to prevent the acoustic waves from reflecting into the ROI and result in a higher SPL reading at the monitoring points.

An initial steady state solution is obtained using the k-ω turbulence model with low under-relaxation factors and low order discretization schemes. Once a steady flow field is obtained, the simulation is switched to transient mode and the SBES shielding function is implemented. The transient solution is obtained in multiple stages, with the first stages run with a coarse time step to flush the flow over the vehicle a number of times such that the flow parameters are allowed to settle. After a simulation time of 2s, the is sampled and recorded to be post processed. It is vital that the data is sampled only when there is no further change in the time step since the FFT can only handle a constant sampling interval.

The Pressure readings are recorded at predetermined locations and is post processed using a built in FFT method. The Overall SPL is extracted by using the defined field functions as mentioned in equation 4.6.

Table 4.2: Solver Settings

Turbulence Model	SBES k-ω SST
Pressure-Velocity Coupling	SIMPLEC
Gradient Scheme	Least Squared Cell Based
Pressure Discretization	Standard
Momentum Discretization	Bounded Central Differencing
K Discretization	Second Order Upwind
ω Discretization	Second Order Upwind
Total Simulation time (s)	4
Simulation time step (s)	$1.25e^{-4}$
Inner Iterations	4

The Turbulence model used is a hybrid SBES model which switches between the LES Turbulence model and the RANS turbulence model based on the location in the flow field. As observed in figure 4.6, the regions close to the wall are modelled using RANS and the regions away from the walls are modelled using LES, to capture the larger and more dynamic turbulent scales.

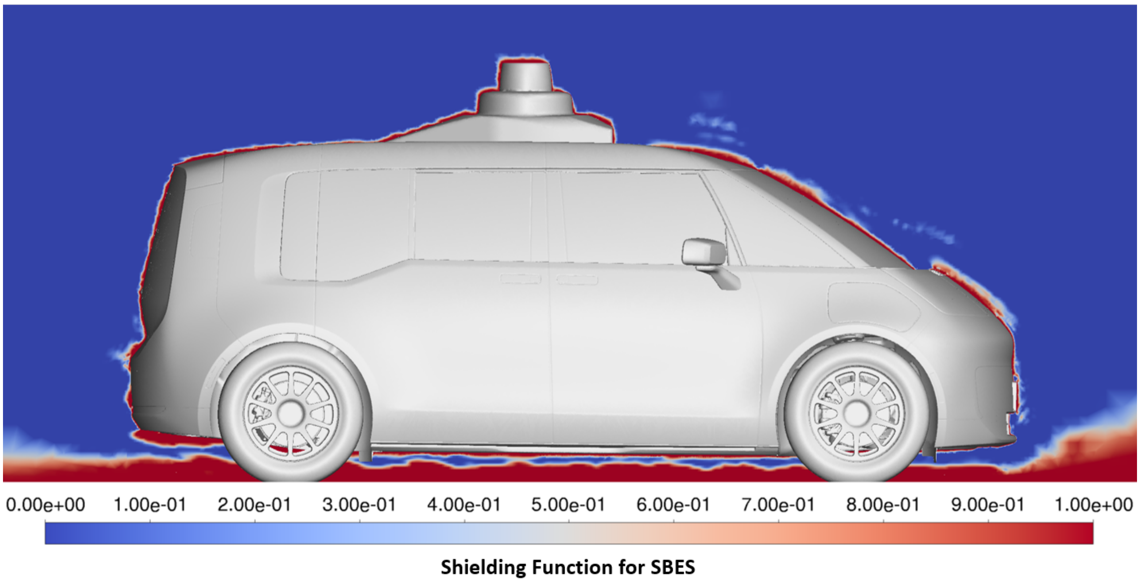

Figure 4.6: The Shielding function of SBES where the blue sections represent LES regions and the Red regions represent RANS regions

4.4.4 Yaw Simulation Setup

The yaw simulations were executed by changing one of the side boundaries from a symmetry boundary condition to a velocity inlet. The side boundary that is opposite to the newly configured velocity inlet was set to a pressure outlet. The choice of which boundary to set as the inlet and outlet is made by the user on the basis of whether a negative yaw angle or a positive yaw angle is desired.

The resulting velocity V_{res} for the yaw simulation is the resultant vector sum of the side wind V_{sw} and the forward velocity of the vehicle V_{veh}. The simulation was run such that the resulting velocity V_{res} is always equal to 130 km/h.

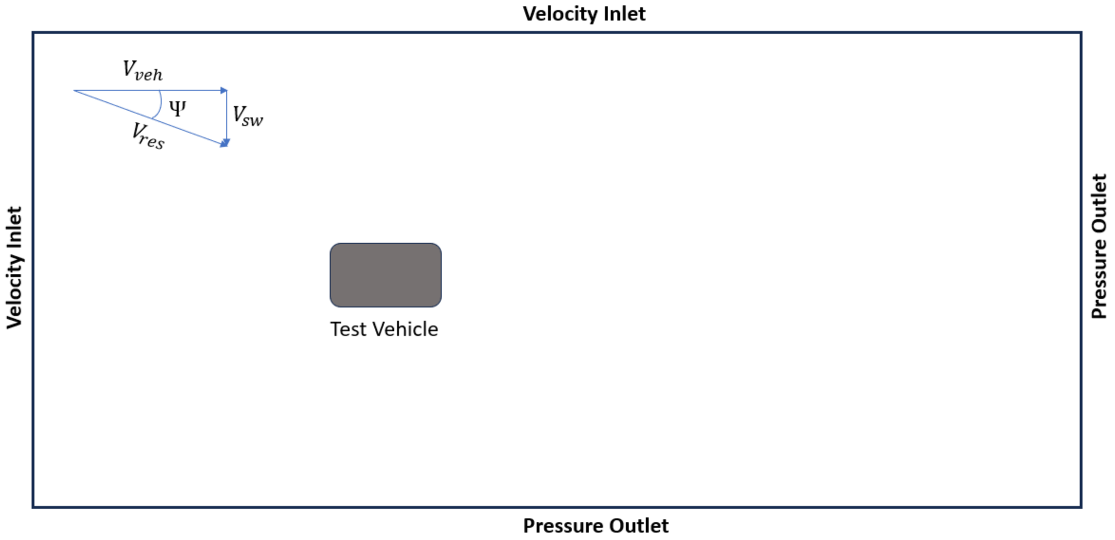

Figure 4.7: A general Yaw simulation setup

4.4.5 Delta Comparison

A delta comparison between the configurations is used to compare the simulation results to the experiment. The delta is defined as the changed configuration SPL [dB] subtracted by the baseline SPL [dB]. A taped configuration without wipers is chosen as the baseline for the simulation and wind tunnel test. This configuration is used to measure a delta when compared to another configuration, e.g. yawed vehicle or folded mirror. A change in the noise perceived due to an altered configuration should correspond to a proportional change in the simulations, when compared with the baseline in both cases.

$$SPL_{Delta} = SPL_{ChangedConfig} - SPL_{BaselineConfig} \tag{4.2}$$

4.4.6 Simulation Error

The simulation error was computed based on two main aspects. The first being the difference between two similar CFD set ups, and the second being the difference between sampling intervals.

4.4.6.1 Sampling Interval

The simulation results were sampled from 2-4 seconds. A comparison to the results captured from the same simulation but during 6-8 seconds is shown below. The higher values of OASPL are marked in red while the lower values of OASPL are marked in green.

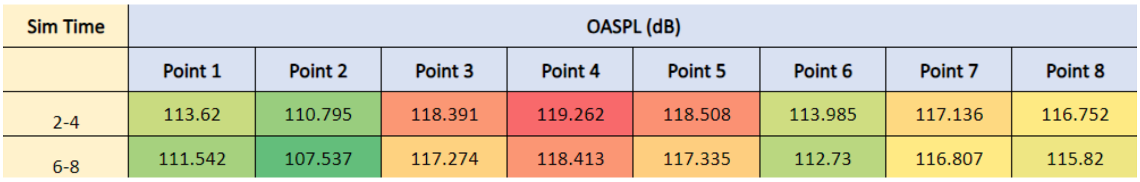

Sim Time	OASPL (dB)							
	Point 1	Point 2	Point 3	Point 4	Point 5	Point 6	Point 7	Point 8
2-4	113.62	110.795	118.391	119.262	118.508	113.985	117.136	116.752
6-8	111.542	107.537	117.274	118.413	117.335	112.73	116.807	115.82

Figure 4.8: The difference in OASPL between 2-4 second and 6-8 second sampling interval. The location of the points are according to figure 4.3.

As seen in figure 4.8, the difference between sampling intervals ranges from 0.33 dB to 3.25 dB. The average error margin was determined to be 1.37 dB.

4.4.6.2 Propagation of error

The propagation of error is defined as the effect of the uncertainty on a scalar quantity [26]. Propagation of error is used to calculate the uncertainty contribution of two or more variables of uncertainty when the variables are added or subtracted. In this case, it will be used to calculate the uncertainty for the delta comparison:

$$\sigma_{total} = \sqrt{\sigma_1^2 + \sigma_2^2 + ... + \sigma_n^2} \tag{4.3}$$

Since the delta comparisons variables have the same unit and individual uncertainty level, the combined uncertainty can be concatenated as follows,

$$\sigma_{total} = \sqrt{2\sigma^2} = \sigma\sqrt{2} \tag{4.4}$$

The simulation uncertainty was deduced empirically from different simulation sampling intervals. The uncertainty is 1.37dB. The total uncertainty can be calculated using equation 4.4:

$$\sigma_{total} = 1.94dB \tag{4.5}$$

4.4.7 User Defined Functions

The OASPL plots were extracted by means of defining a user defined function and plotting the values over the vehicle, given by the equation 4.6

$$OASPL(dB) = 20log_{10}(\frac{P'_{RMS}}{P_{ref}}) \tag{4.6}$$

Where P_{ref} is the reference pressure corresponding to the lowest threshold of hearing [8]. P'_{rms} is the RMS value of of the Static Pressure fluctuations in the domain. Given by the equation 4.7

$$P'_{RMS} = \sqrt{\frac{1}{T} * \int_0^T [P'(t)]^2} \tag{4.7}$$

However P'_{RMS} can aslo be extracted using the mean of the static pressure squared.

$$\overline{P^2} = \overline{(\overline{P} + P')^2} \tag{4.8}$$

The Static pressure P consists of a Mean component $\overline{P}$ and a fluctuating component P'. Solving for the root of the Pressure fluctuations squared, we can obtain a formula for the RMS of the pressure fluctuations. In order to extract the mean values, data sampling needs to be switched on during the solution phase of the simulation.

$$\sqrt{\overline{P'^2}} = \sqrt{\overline{P^2} - \overline{P}^2} \tag{4.9}$$

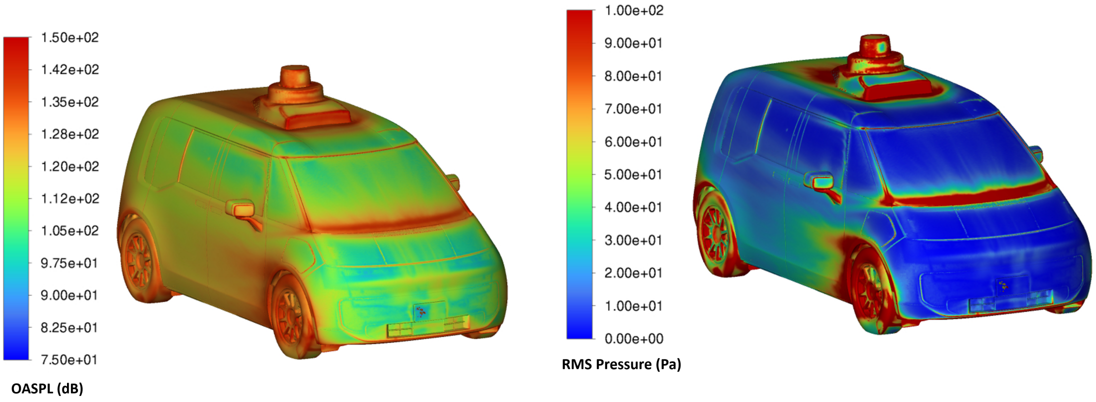

(a) OASPL Plot **(b)** RMS Pressure Plot

Figure 4.9: Custom Field Function Plots

4.4.8 Acoustics Post Processing

4.4.8.1 Surface Reports

When analysis discrete points in the side window and quarter glasss, there is a strong possibiliy that the points can be located in regions of high turbulent activity which may not always have a correlation to the noise measured by the accelerometers on the inside of the side window and quarter glass. A linear averaging method was implemented for the experimental data and a area weighted surface average was implemented as seen in equation 4.10. Through this comparison, it was found that surface-averaged SPL measurements provided more comprehensive readings as opposed to the point pressure monitoring as displayed in figure 4.3. The area-weighted average of a quantity ϕ over a surface is given by:

$$\langle \phi \rangle_{\text{aw}} = \frac{1}{A} \sum_{i=1}^{N} \phi_i |A_i| \tag{4.10}$$

where:

- $\langle \phi \rangle_{\text{aw}}$ is the area-weighted average of the quantity ϕ.
- N is the number of surface elements (or cells) over which the averaging is performed.
- ϕ_i is the value of the quantity ϕ at the i-th surface element.
- A_i is the area of the i-th surface element.

The averaging will be done over the whole quarter glass and side window. This will give a more accurate comparison to the experimental data as more data is incorporated from the simulations in the comparison. Much like the experimental data where vibration at one point on the glass affects vibration at another point, the overall pressure fluctuations experienced on the green-house panel is now affected by the whole surface rather than just two discretized points. These simulation results are representative of a wider array of data, making them more comparable.

4.4.8.2 Fast Fourier Transform

The Static Pressure in the ROI is logged as a time series data over the duration of the simulation solution. From this data, the pressure can be plotted with respect to time. A FFT algorithm is implemented using an in built tool which generates the frequency spectrum of the SPL, extracted using the reference pressure P_{ref} of 20 μPa, as observed in figure 4.10. However since the FFT algorithm assumes that the signal is infinitely repeating, a windowing function needs to be appled such that the signal starts and ends at zero amplitude. For this purpose, the Hanning windowing function with an overlap of 67% was used. The resultant frequency spectrum is split into its constituent 1/3 Octave bands for a more detailed analysis of the primary contributor to the noise generated by the vehicle.

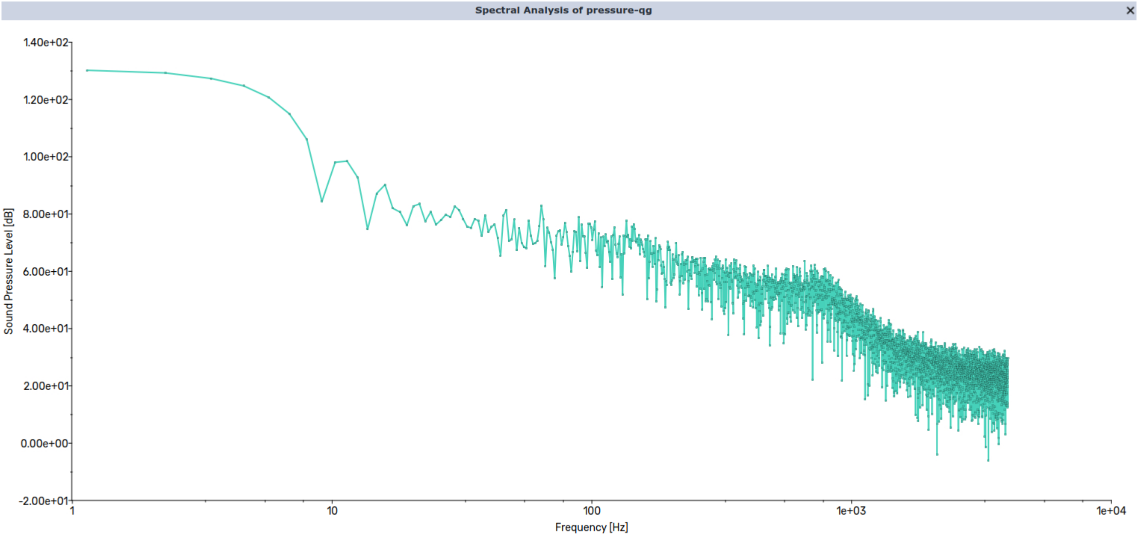

Figure 4.10: Frequency Spectral analysis of the pressure readings on the Quarter glass

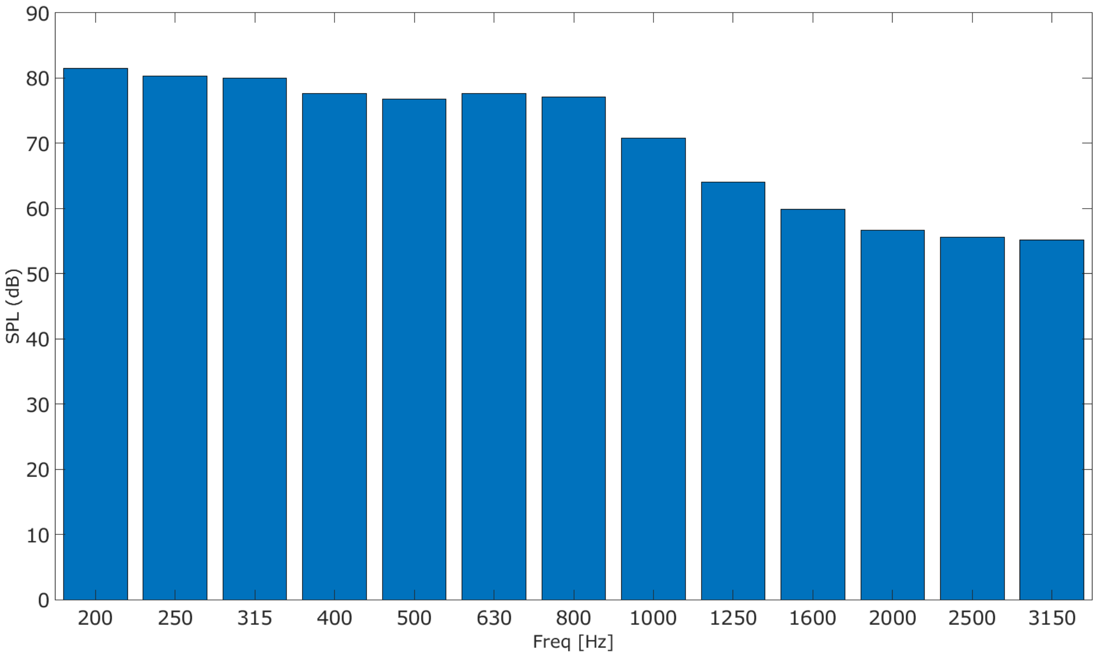

Figure 4.11: The frequency spectrum from figure 4.10 split into 1/3 Octaves.

4.4.9 Computational Mesh

The base mesh primarily consists of a hexahedral mesh with refinements around the ROI. The simplified test object facilitates a simpler mesh due to the flat underbody and the closed underhood flow and consequently minimises simulation time. The computational mesh consists of an offset surface for the whole vehicle which was assigned a specific cell size. The ROI for the subsequent tests were set to the an

Method	Fast Fourier Transform
Windowing	Hanning
Overlap	0.67
Sampling Frequency	8000 Hz
Maximum Resolved Frequency	3150 Hz

Table 4.3: Acoustic Post Processing Settings

offset surface that encompasses the left hand side view mirror, quarter glass and side window. The cell size within this offest surface was investigated in the mesh study. A mesh with no additional refinements consists of $82 \cdot 10^6$ elements.

For this study a y^+ value of under 5 is desired to obtain accurate and reliable numerical results near the wall regions [25]. The computational mesh was designed such that the target wall y^+ was under 1 in the ROI and the noise transmission region, which is typically the surfaces that generate a high amount of vortices such as the A-pillars and the side view mirrors [7], while the target y^+ over the whole vehicle exterior was set to be under 5 as seen in figure 4.12. The brake discs and suspension geometry was set to have a high y^+ due to those components not being affected by the flow to the same extent as the external body.

Table 4.4: Custom Mesh Controls

Region	**External Body**	**ROI**	**A-Pillar and Mirror**
Base Size (mm)	12	3	12
Number of Prism Layers	12	12	14
Prism Layer near wall thickness (mm)	0.03	0.03	0.01

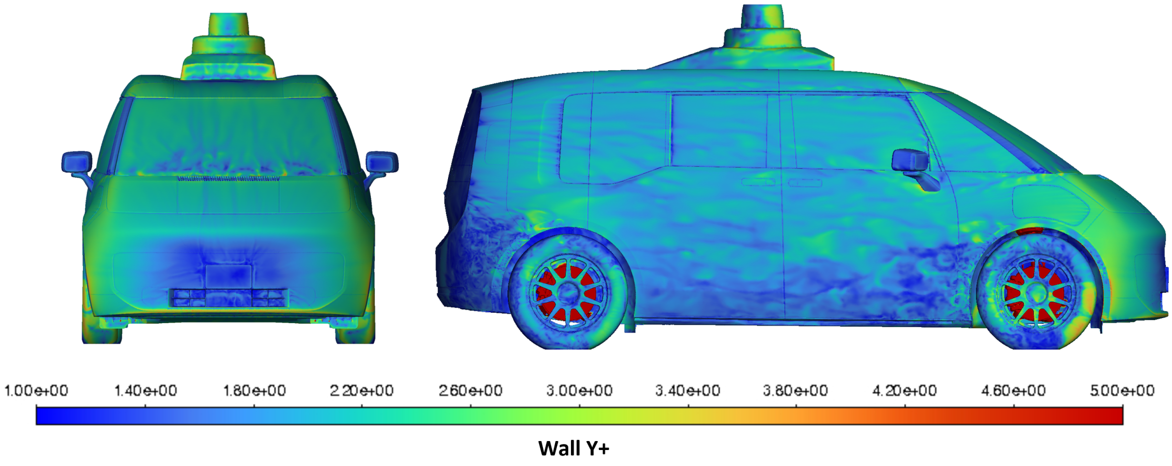

Figure 4.12: Wall y^+ plotted over the surface of the entire vehicle.

4.4.10 Mesh and Time Study

A series of mesh, time step and simulation time studies have been performed to evaluate the effects of each setup on the simulation results. The goal is to find the limit where refining the mesh or the time step further will no longer yield a significant change in the result to justify the increased computational cost that accompanies it. To draw meaningful inferences between the different comparisons, a metric defined as OASPL (Overall Sound Pressure Level) is used. This gives a general indication about the intensity of the sound simulated by the CFD solver. The following section explains in detail the subsequent studies that have been carried out.

4.4.10.1 Wake Refinement

A wake refinement study was carried out to evaluate whether or not a refinement downstream of the would affect the results in the ROI as seen in the figure 4.13.

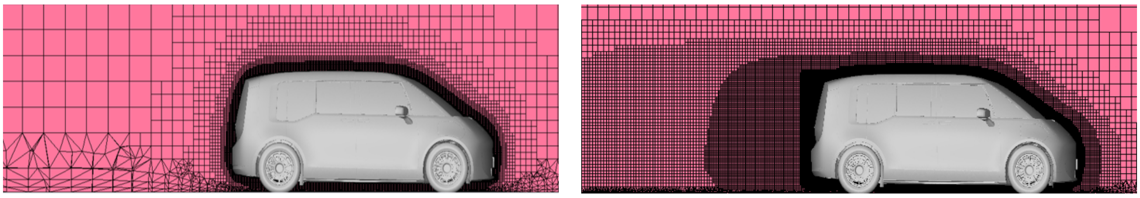

(a) Computational Mesh without wake **(b)** Computational Mesh with wake

Figure 4.13: Wake study comparison

From the plots in the figure 4.14 it can be inferred that the change in the OASPL measured do not vary significantly with the wake refinement. Hence it can be concluded that the wake refinement would not have a significant effect on the results at the monitoring points. The wake refinement would add around $10 \cdot 10^6$ cells, about 12.5 % more cells than the baseline. Hence saving additional computational costs.

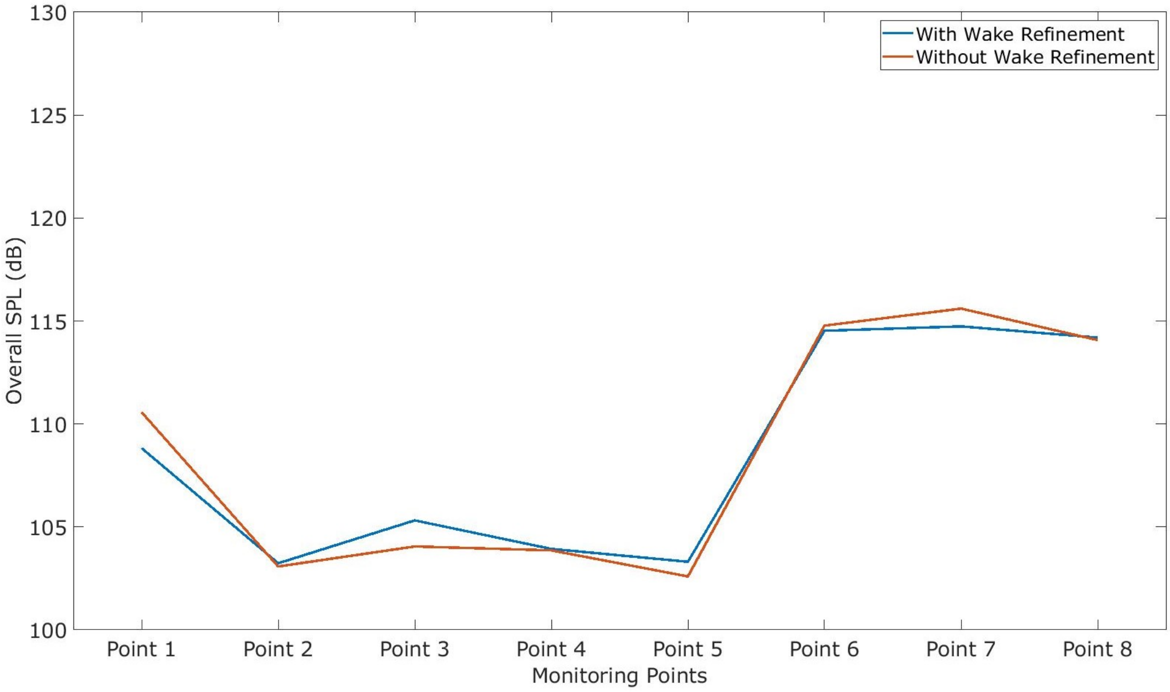

Figure 4.14: The OASPL evaluated at measuring points with and without wake refinement

4.4.10.2 ROI Refinement Box

A mesh refinement study was carried out on the ROI. The PIDs for the ROI were selected, in this case the ROI was selected to be the left A-Pillar, Left Quarterglass and window and the left Outside Rear View Mirror. An offset surface of 200 mm extending externally was created. The pressure waves need to be adequately resolved in space, the general recommendation is around 15 to 20 grids per smallest wavelength, see equation 2.14. A finer mesh would resolve the waves better in time but however there is a limit that exists where refining the mesh further would yield no significant change in the results.

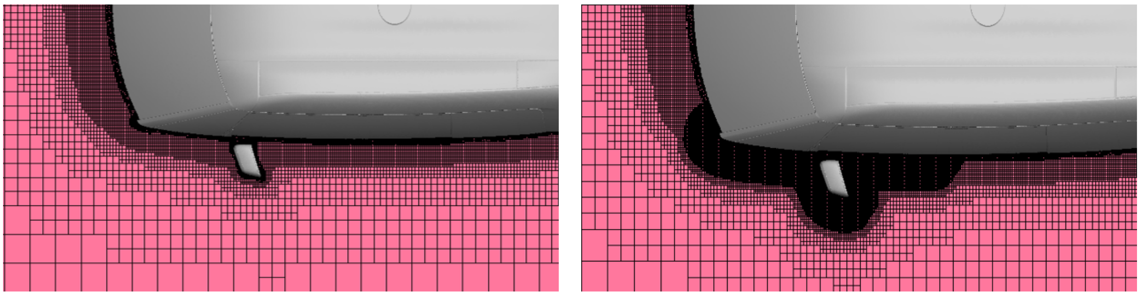

(a) Computational Mesh without ROI refinement

(b) Computational Mesh with 3mm ROI refinement

Figure 4.15: Wake Study Comparison

As seen in figure 4.15, a mesh refinement in the ROI resolves significantly more sound the finer the mesh, due to more of the turbulent eddies resolved in LES mode. A gradual increase can be observed in the OASPL values for each refinement step, especially from point 1 to point 5. Which is due to the turbulent eddies being better resolved with the finer mesh. The 1.5mm refinement was observed to resolve the most sound however at the cost of substantially higher resources as observed in the plot 4.17 For subsequent studies, the 3mm ROI refinement was selected.

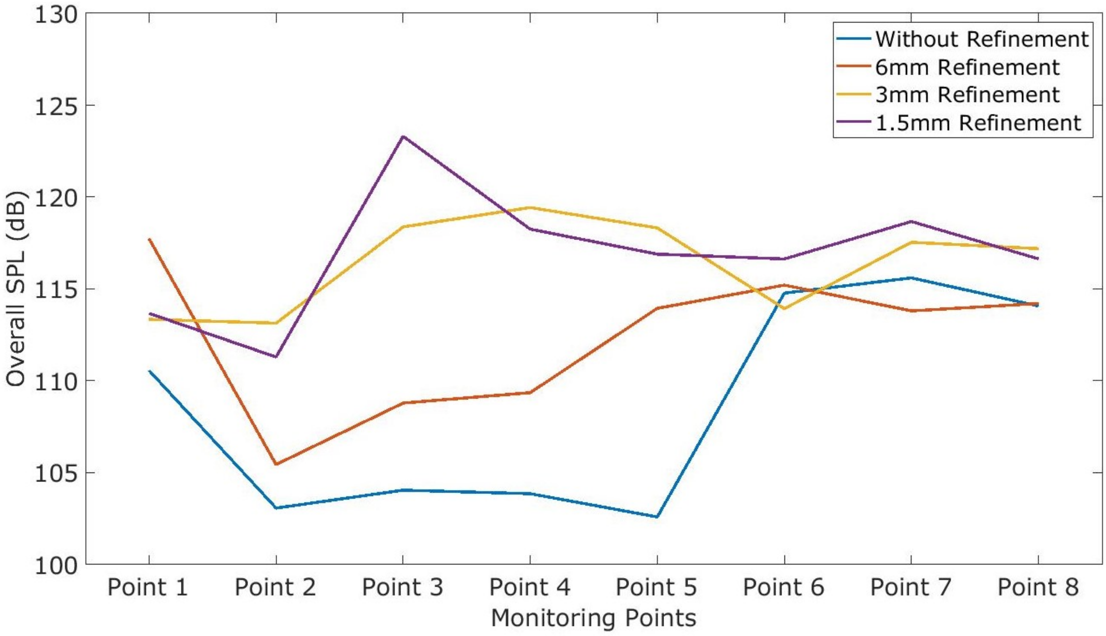

Figure 4.16: The OASPL evaluated at measuring points with refinement at the region of interest around the side window, quarter glass and mirror.

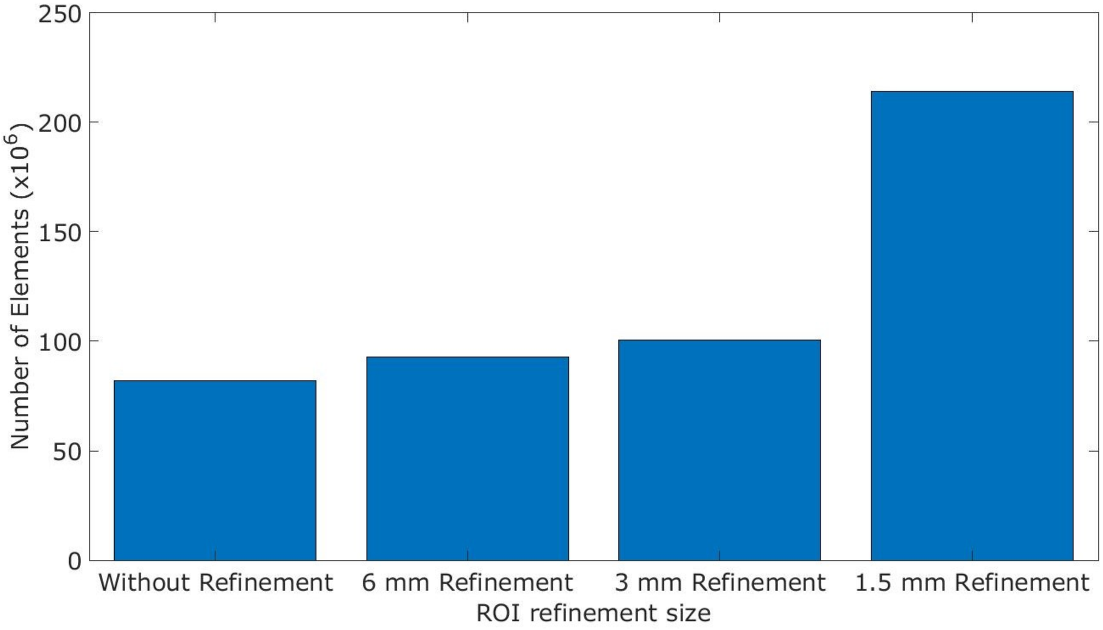

Figure 4.17: The number of elements in millions for each base size of the region of interest around the side window, quarter glass and mirror.

4.4.10.3 Simulation Time Study

The simulation was run for a total time of 2.75s, 4s, 6s and 8s. This includes a ramp up phase where the transient simulation is run with a large time step to flush the flow across the domain. The data is sampled after 2s, when the flow has been allowed to settle. The longer the simulation has run, the more number of data samples are analyzed though this inevitably comes at the cost of resources.

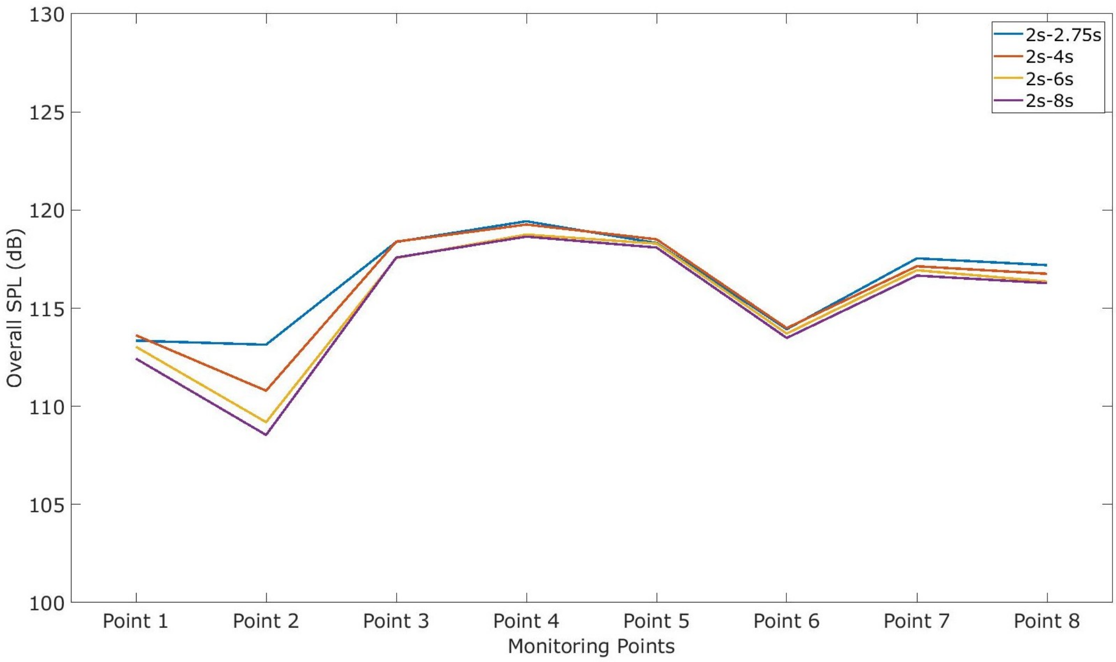

Figure 4.18: The OASPL evaluated at measuring points with varying simulation times

It can be observed from figure 4.18, there is a marginal decrease in the simulated OASPL in the side window from point 3 to point 6 and a more significant change in the OASPL in the quarter glass corresponding to point 1 and point 2 as the time simulation time is increased. The observed change for all the points when the simulation was extended from 4s to 8s was within the predetermined numerical error margin, therefore justifying the choice to select 4s as the simulation time for subsequent simulations.

4.4.10.4 Simulation Time step Study

The simulation was run with time steps of 0.5 ms, 0.25 ms, 0.125 ms, 0.0625 ms. The data is sampled once per time step, with a lower time step resulting in a higher sampling frequency and a higher frequency resolution, in accordance to the Nyquist-Shannon theorem [19]. The maximum frequency resolved is 1/2.56 times the sampling frequency. Concluding that a lower time step would be able to resolve a higher frequency.

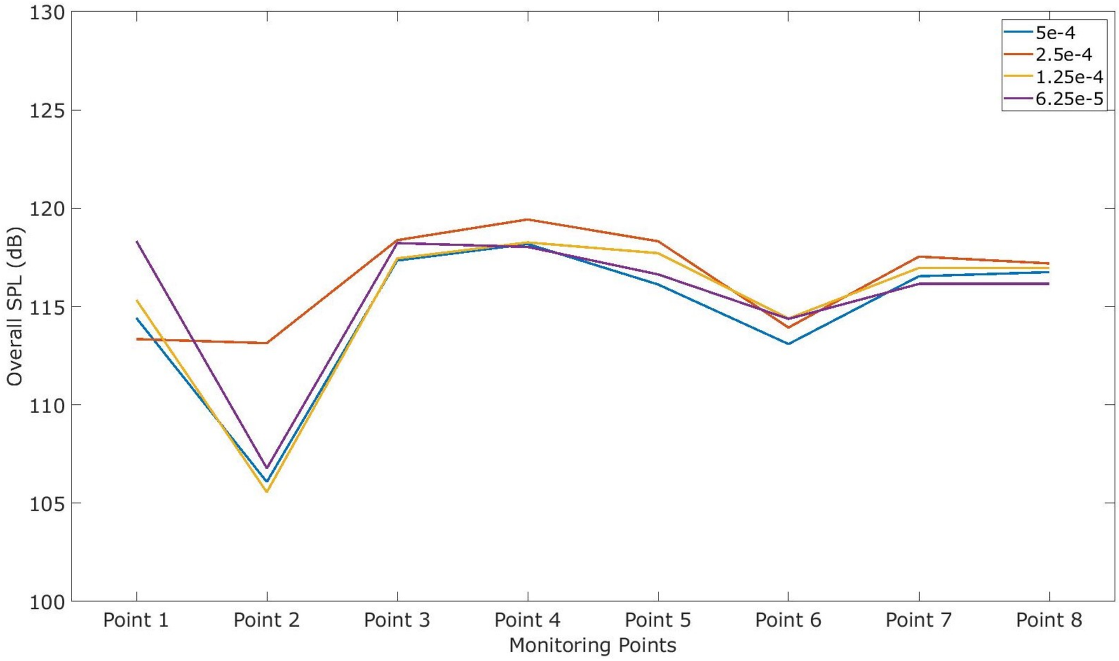

Figure 4.19: The OASPL evaluated at measuring points with varying simulation time steps

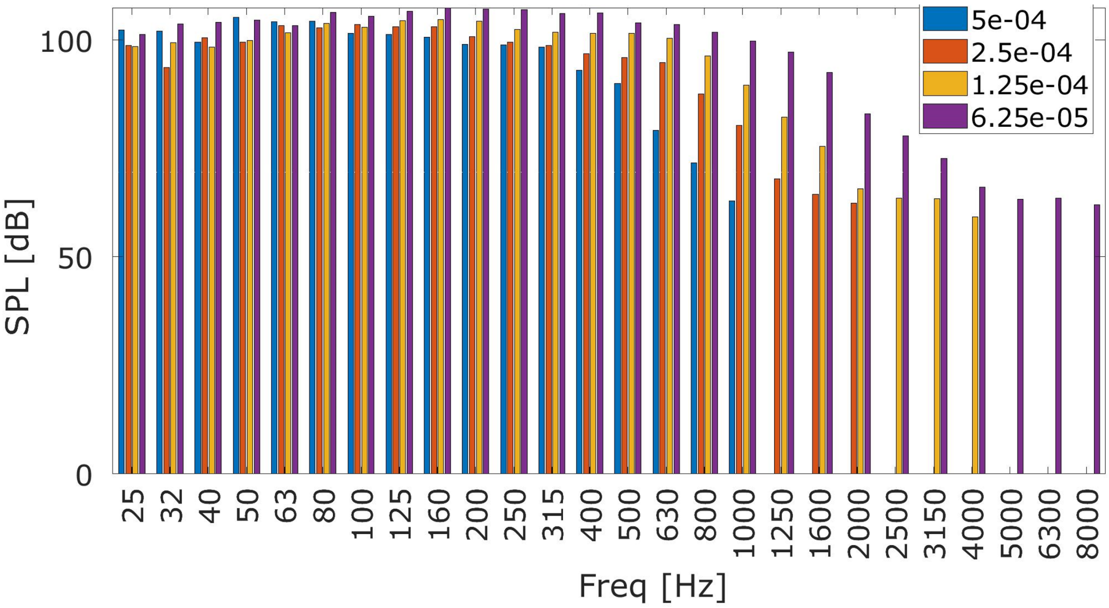

Figure 4.20: The SPL measured with different time steps

Though the human ear can perceive sound from 20 Hz to 20,000 Hz, it is however most sensitive to frequencies betweem 1,000 Hz and 6,000 Hz [27]. For this study, the resolved frequency is limited to 8,000 Hz. As observed in figure 4.19 there is a slight change in the OASPL from point 3 to point 8, corresponding to the side window. Although there was no significant change observed in the overall sound pressure levels, we can clearly observe the effects of aliasing with a smaller time step when a frequency analysis is carried out, as observed in figure 4.20. Aliasing occours when a wave is inadequately sampled in the time domain. A decrease in the SPL resolved can be observed as the maximum resolved frequency (F_R) approaches 1/2.56 times that of the sampling frequency ($F_S/2.56$). A smaller time step would also resolve the high frequency turbulent eddies more accurately hence contributing to a more more representative data set. A decrease in the time step by a factor of 2 would lead to the simulation time doubling. For subsequent studies, a time step of 0.125 ms was selected as it proved to be a good trade off between simulation time and accuracy.

5

Results and Discussion

The following section consists of details pertaining to the results obtained over the course of the study.

5.1 Correlation with wind tunnel data

A critical aspect of the method development is to evaluate how closely the simulation data correlates with the data from the physical wind tunnel test. This validation is conducted to verify the accuracy of simulations, ensuring that they are comparable to real-world results. A like-to-like comparison between configurations is challenging due to the vast difference in set-up between the wind tunnel and simulation. For an example, the wind tunnel may measure additional noise caused by the wind tunnel, such as fan noise, or there may be blockage in the tunnel caused by the size and shape of the wind tunnel that could affect accelerometer readings [4]. These conditions are not present in the simulation and hinder a direct comparison to the experimental results.

The simulation setup deos not have any effects due to blockage on the flow. The expansive domain allows the air stream to compress and decompress around the vehicle realistically, without interference from external structures such as wind tunnel boundaries. Consequently, the results are more representative of actual road conditions rather than wind tunnel conditions. The confined space of the wind tunnel may adversely affect the experimental results due to acoustic reflections while the implementation of a symmetry boundary condition on the side walls ensure that no acoustic noise is reflected back into the ROI, further resembling road conditions. In yawed cases, the vehicle may induce more blockage around its sides, compressing more flow and affecting the behavior around critical turbulent structures such as the side mirrors and A-pillars. This could obscure flow patterns crucial to accurate experimental measurements.

Even after taking the difference in setup between the simulation and the wind tunnel test, there is a fundamental difference in the method of extracting the sound. In the physical wind tunnel test, glass vibrations were measured using accelerometers to measure vibrations on the inside of the glass as opposed to the simulation, where pressure fluctuations were measured on the outside of the glass. It is not physically sound to directly compare absolute levels of pressure differences in air to

Configuration number	Description	Yaw Angle (deg)
1	Baseline	-20
2	Baseline	-10
3	Baseline	0
4	Baseline	+10
5	Baseline	+20
6	Folded Mirror	0
7	With Wipers	0

Table 5.1: Configurations tested both in the wind tunnel and simulations

accelerations in a solid medium such as glass without a vibro-acoustic model. Such a model allows the propagation of the sound from the air to the glass to be realized. Without it, however, it is difficult to predict the vibrational behavior of the glass and consequently make a like to like comparison.

Despite the differing fundamental units, it is possible to compare the experimental and numerical results using a delta comparison in decibels. The glass is assumed to have a linear transmission of sound across all frequencies, meaning that vibrations increase linearly. This implies that a linear increase in pressure fluctuations produces a linear increase in vibrations in the glass. Therefore, while the absolute values are not directly comparable, the delta between configurations can be effectively compared and evaluated.

Since the glass acts as a transmission medium, a particularly high level of vibration recorded at one point can still have an effect on another point on the window, whereas this phenomena remains relatively isolated when it comes to the monitoring points in the simulation. A high SPL reading on one point may not necessarily have an effect on another point at the other end of the window.

The configurations used for obtaining the correlation with the wind tunnel data are listed in the table 5.1. The baseline does not have windshield wipers, panel gaps and taped grilles for the cooling and HVAC (Heating Ventilation and Cooling) systems. The panel gaps are taped in order to remove the noise that would be created by the turbulence, which would otherwise be wrapped in the CFD simulation. The "Folded Mirrors" configuration suggests that the mirrors are folded towards the window.

5.1.1 Yaw Simulation Comparisons

For the correlation study, the Yaw simulations proved to be interesting since the increased velocity and mass-flow over the A-pillars proved to have a general increase in the noise levels in the experimental data. A positive yaw angle implies that the vehicle is rotated clockwise when viewed from above, and counter-clockwise for negative yaw angles as seen in figure 5.1.

The physical implication of this effect on the monitors was that a higher SPL was observed in both simulations and experiments. A more detailed analysis follows.

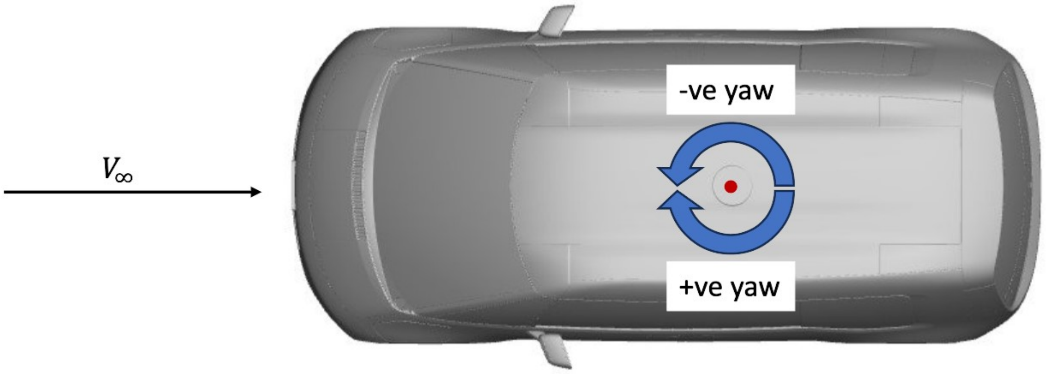

Figure 5.1: Yaw simulation naming convention

5.1.1.1 -20°Yaw

For a yaw angle of Ψ = -20°, a higher SPL delta can be observed for all frequency bands compared to the baseline configuration, which signifies that this configuration yields an increase in the intensity of the measured and simulated noise.

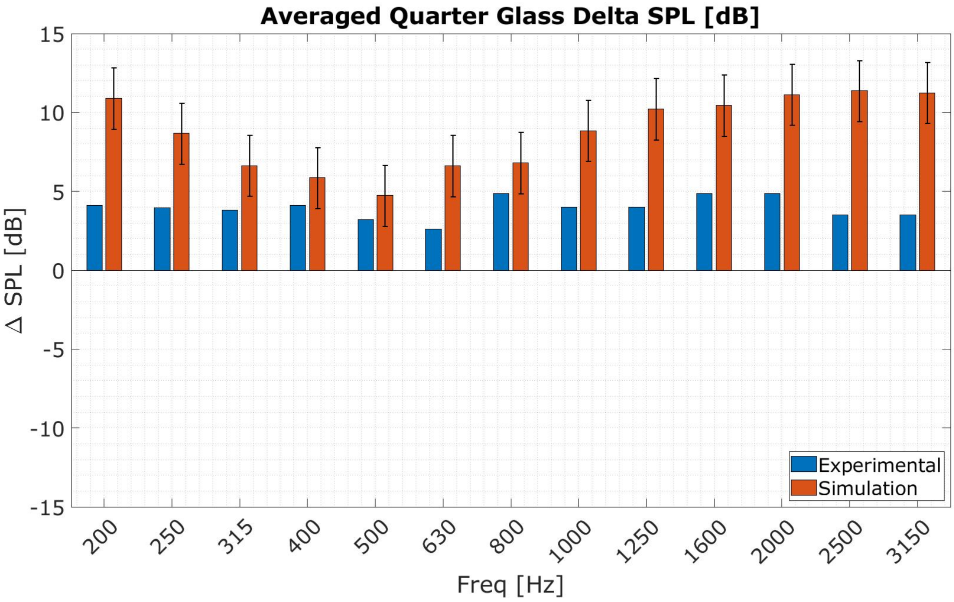

(a) Averaged delta SPL for the quarter glass.

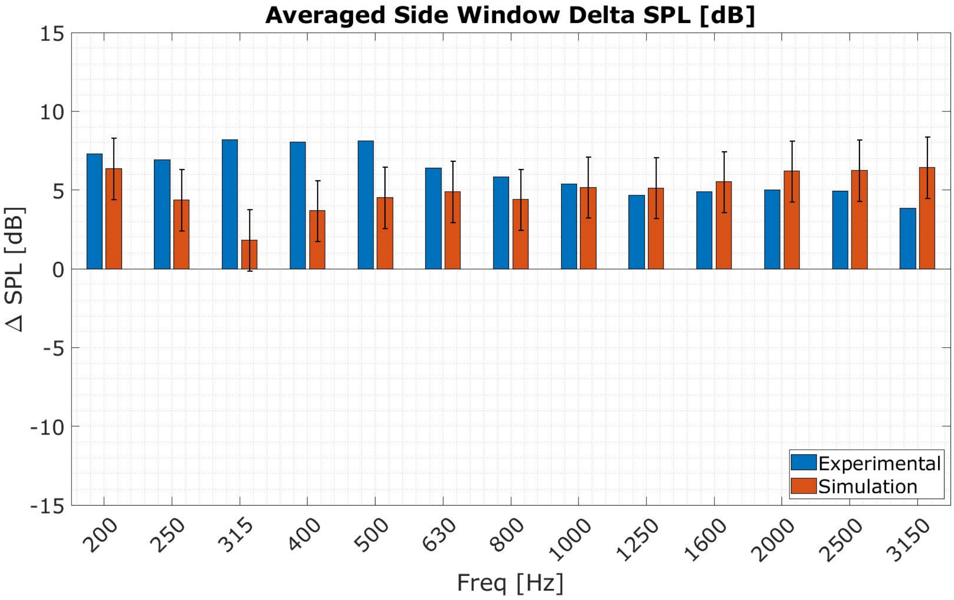

(b) Averaged delta SPL for the side window.

Figure 5.2: Experimental vs. Simulation Delta between the -20°yaw and the baseline configuration for the quarter glass 5.2a) and side window 5.2b).

Figure 5.2a suggests that the simulation predicts a greater SPL on the quarter glass compared to the wind tunnel data. This could be the results of the differences between the set up in the wind tunnel and the simulation. The wind tunnel has walls that constrict the true flow around the vehicle. This constriction may affect the development of the a-pillar vortex during high yaw cases, resulting in a lower measured SPL. It's important to note, however, that both values still predict the an increase in SPL when yawing the vehicle negatively and are of the same magnitude.

As can be observed in 5.3, the OASPL on the windows are significantly higher than the baseline in the -20 deg yaw case. This is due to the air accelerating around the A-pillars, as observed in the instantaneous velocity plots at 4s 5.4, which leads to a stronger and a more unstable A-pillar vortex that interacts with the quarter glass and a portion of the side window. The increased velocity of the flow around the A-pillar also interacts with the outside rear-view mirror (ORVM) and consequently more unstable turbulent structures are produced which then interacts with the side window and quarter glass, yielding a higher SPL reading.

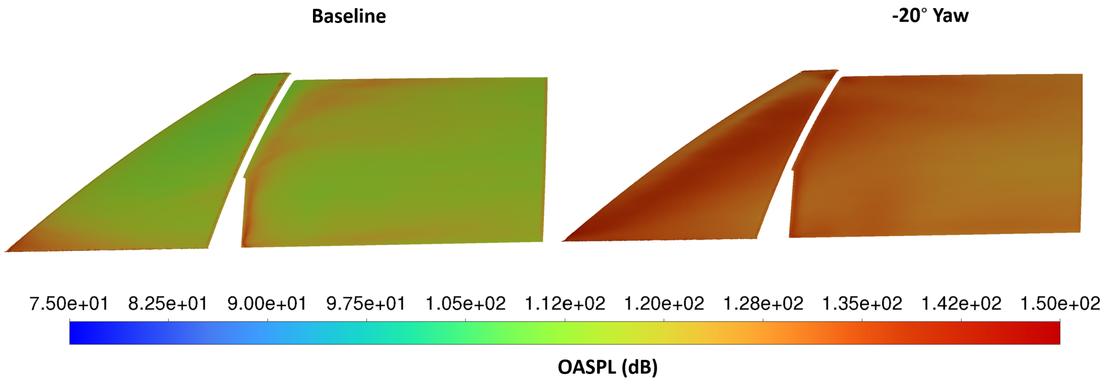

Figure 5.3: A comparison of the OASPL plots at -20°Yaw

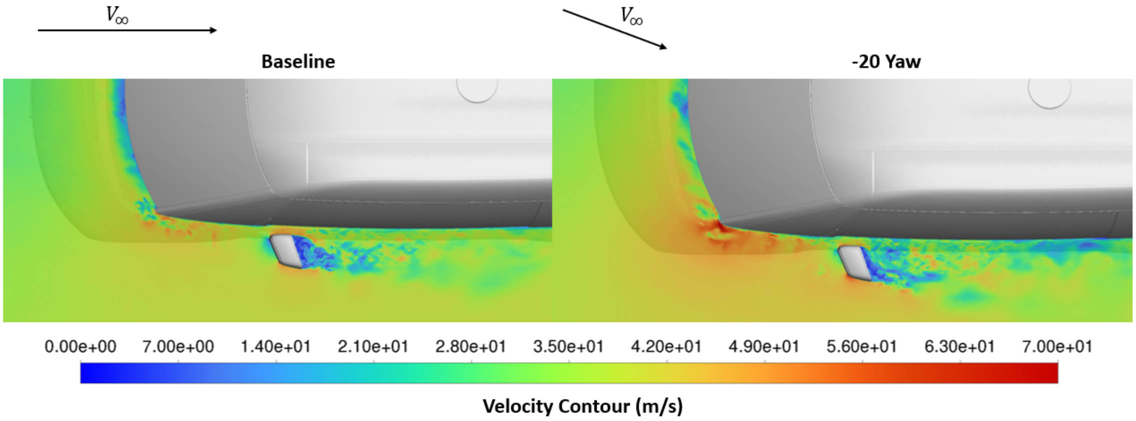

Figure 5.4: A comparison of the Velocity plots at Z = 1.37m at -20°Yaw

5.1.1.2 -10°Yaw

The -10°Yaw case displays similar SPL trends to the experimental wind tunnel results, with an increase in the SPL observed for the delta comparison. The values are all positive and of comparable magnitude, suggesting that the simulation predicts the same phenomena as the experimental data.

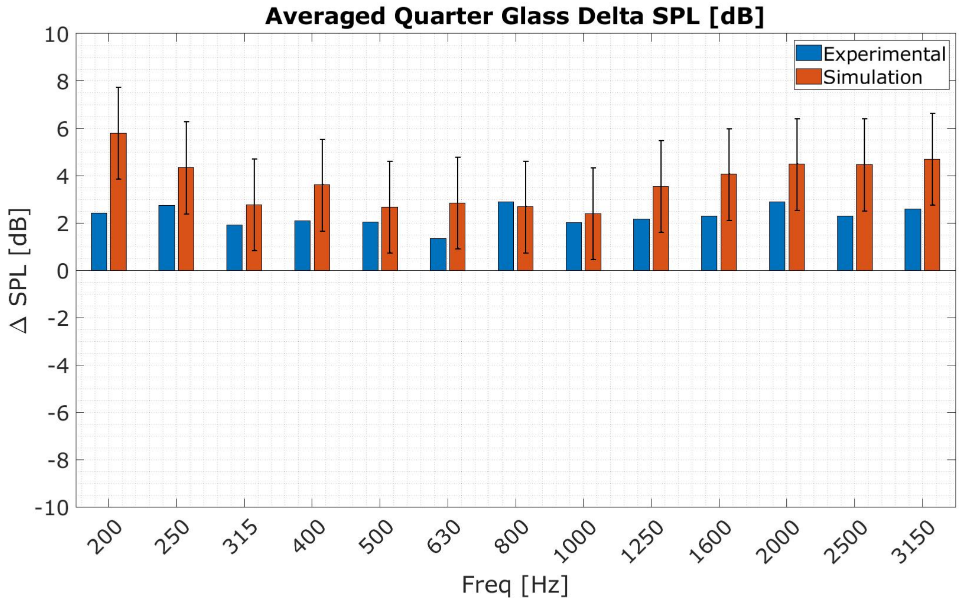

(a) Averaged delta SPL for the quarter glass .

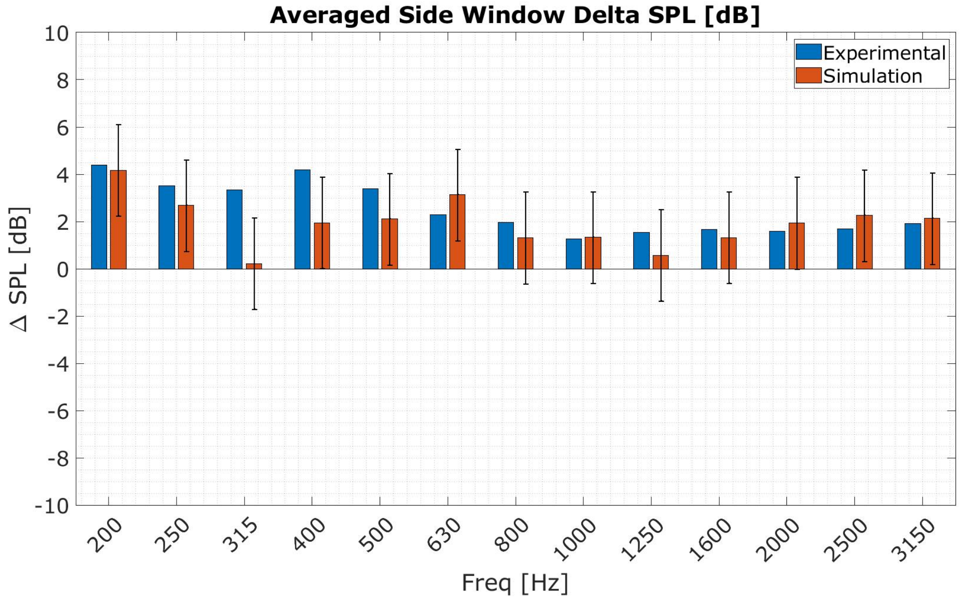

(b) Averaged delta SPL for the side window .

Figure 5.5: Experimental vs. Simulation Delta between the -10°yaw and the baseline configuration for the quarter glass 5.5a and side window 5.5b.

Despite the discrepancy in the delta measurements, the difference between values are within acceptable limits and the delta uncertainty for most third octave bands. This indicates that there is a good level of correlation with the wind tunnel test data.

As observed in figure 5.5a and figure 5.5b, there is an increase in the SPL levels measured when the vehicle yaw angle is ψ = -10. The increase in the OASPL can also observed in figure 5.6 compared to the baseline. This increase can visualised by the darker streak of red that is spotted going across the quarter glass due to the effect of the A-pillar vortex.

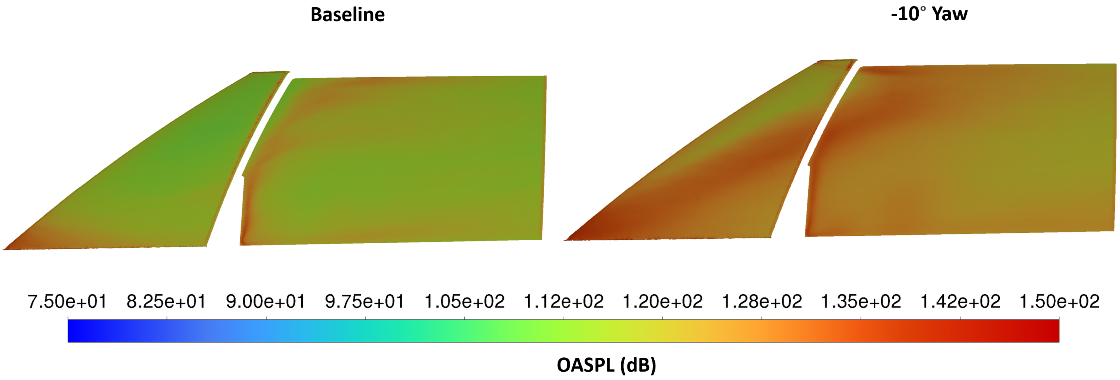

Figure 5.6: A comparison of the OASPL plots at -10°Yaw

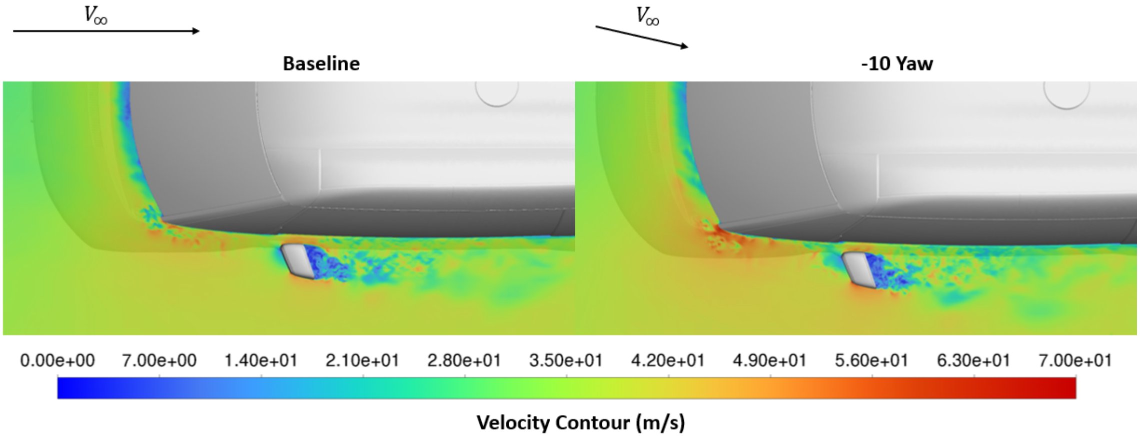

Figure 5.7: A comparison of the Velocity plots at Z = 1.37m at -10°Yaw

5.1.1.3 10°Yaw

A positive yaw angle decreases the SPL on the measured surfaces for both simulation and experimental data. The SPL delta across the frequency bands was observed to be lower when compared to the baseline. However the simulation predicts a higher SPL in the Quarter glass in the frequencies above 2000 Hz. The flow velocity around the A-pillar and the ORVMs were observed to not be as high as the baseline case, which resulted in the A-pillar vortex that is not as strong as compared with the Baseline or the cases with negative yaw.

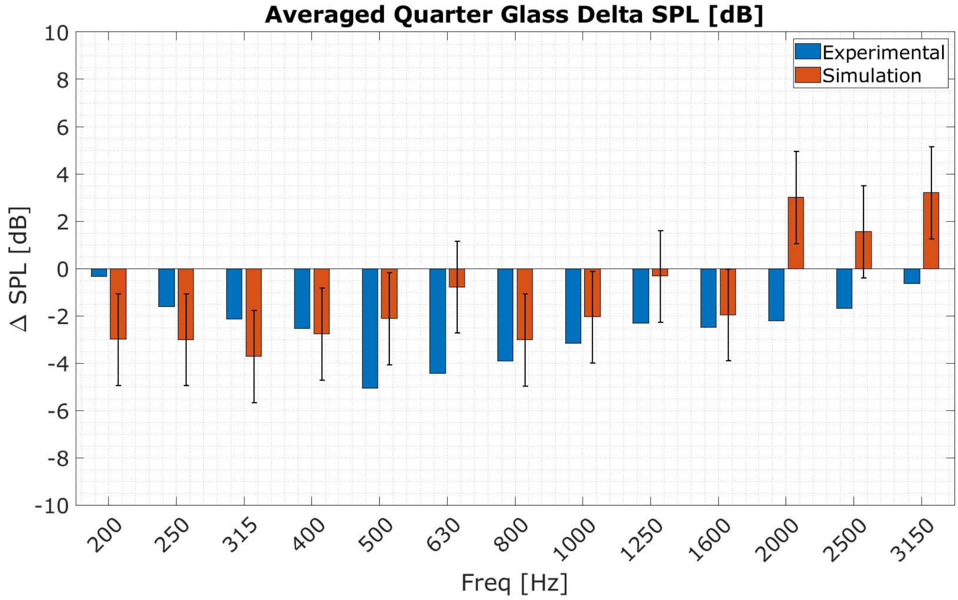

(a) Averaged delta SPL for the quarter glass .

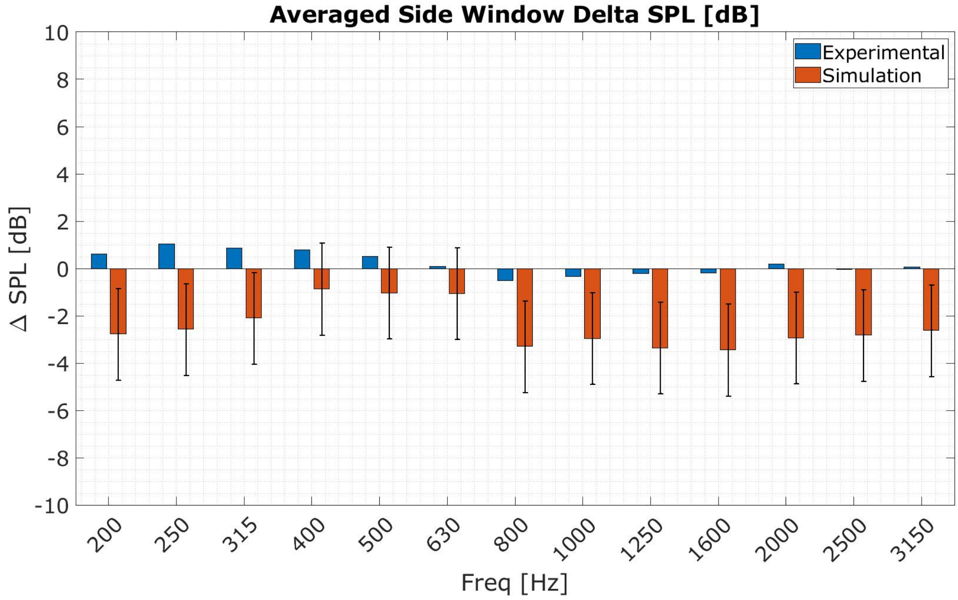

(b) Averaged delta SPL for the side window.

Figure 5.8: Experimental vs. Simulation Delta between the 10°yaw and the baseline configuration for the quarter glass 5.8a
and side window 5.8b.

The experimental data was observed to have a marginal change in the SPL delta on the side window when compared to the simulation. A possible reasoning for this could be that the accelerometers in the positive yaw cases are facing the windward side of the vehicle and hence picks up a lot of ambient noise from the wind tunnel. This ambient noise is much higher in magnitude and hence the change in the noise levels due to the yaw angle is not as significant.

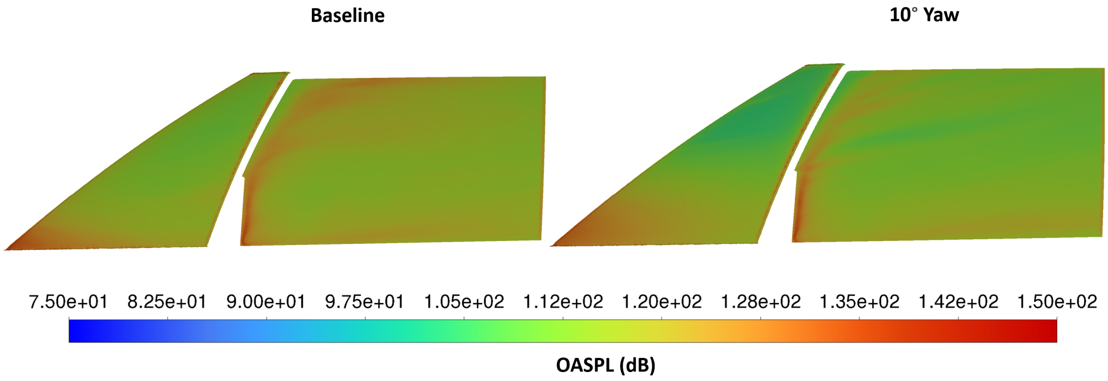

Figure 5.9: A comparison of the OASPL plots at 10°Yaw

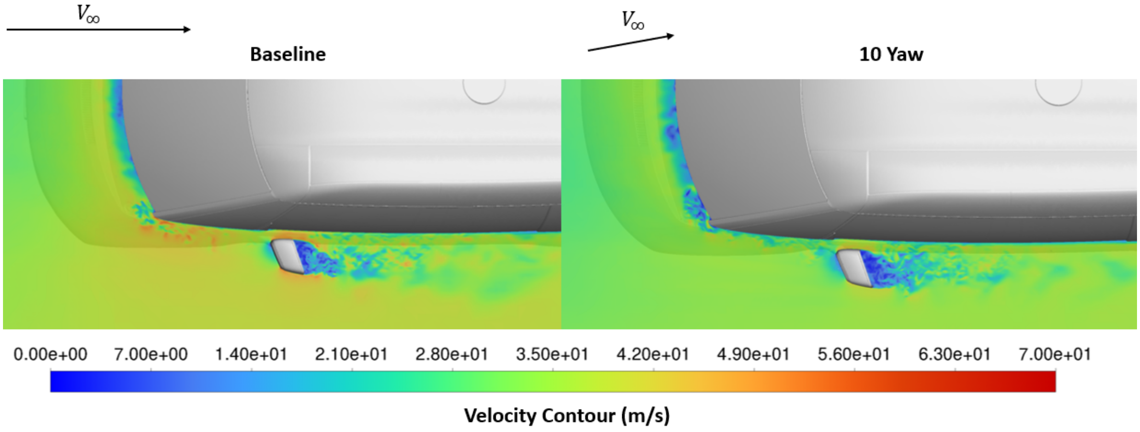

Figure 5.10: A comparison of the Velocity plots at Z = 1.37m at 10°Yaw

Generally a lower SPL level was observed for all the octave bands in the frequency spectrum. This is due to the velocity of flow around the A-pillars not being as high, as evidenced by the figure 5.10. Consequently the A pillar vortex is not as strong and this results in a lower OASPL on the quarter glass and side window as seen in figure 5.9.

5.1.1.4 20°Yaw

The 20°yaw delta displays similar trend as the 10°yaw configuration for the quarter glass, as seen in figure 5.11a. The simulation has a clear decrease in SPL for the 20°yaw configuration which is in line with SPL trends expected for a positively yawed vehicle.

The 20°simulation also seems to predict a greater delta for som frequencies on the quarter glass when compared to the wind tunnel data, as seen on the quarter glass of the -20°simulation. This suggests that the simulations predict a greater value with higher yaw angles. It may also be the result of exposure to the noise of the wind tunnel. As the quarter glass faces the wind tunnel inlet, more noise is picked up by the accelerometers, leading to louder measurements for the positive yaw case and a smaller delta when compared with baseline. Despite the small difference, both experiments and simulation predict a decrease in SPL on the quarter glass when positively yawing the vehicle.

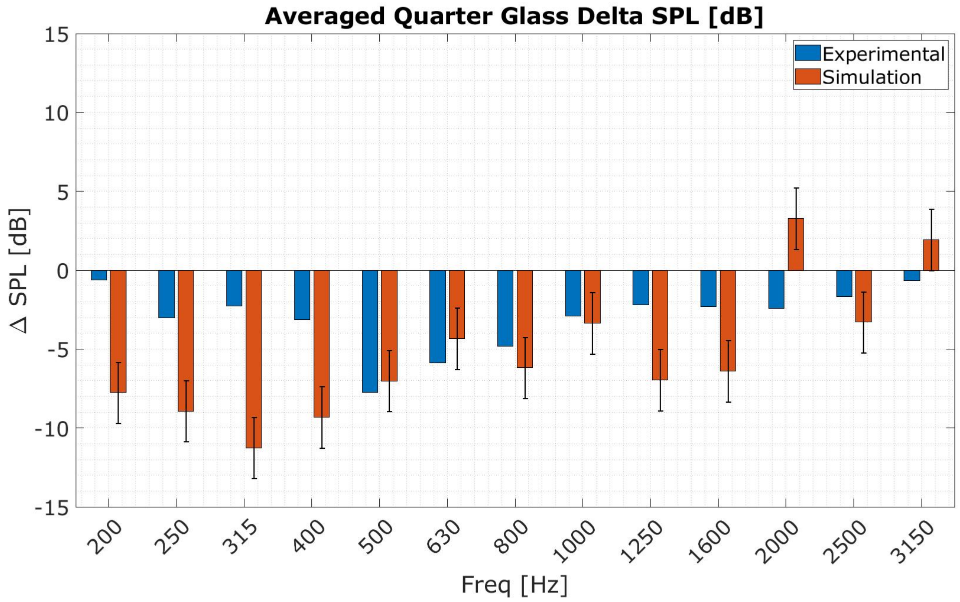

(a) Averaged delta SPL for the quarter glass.

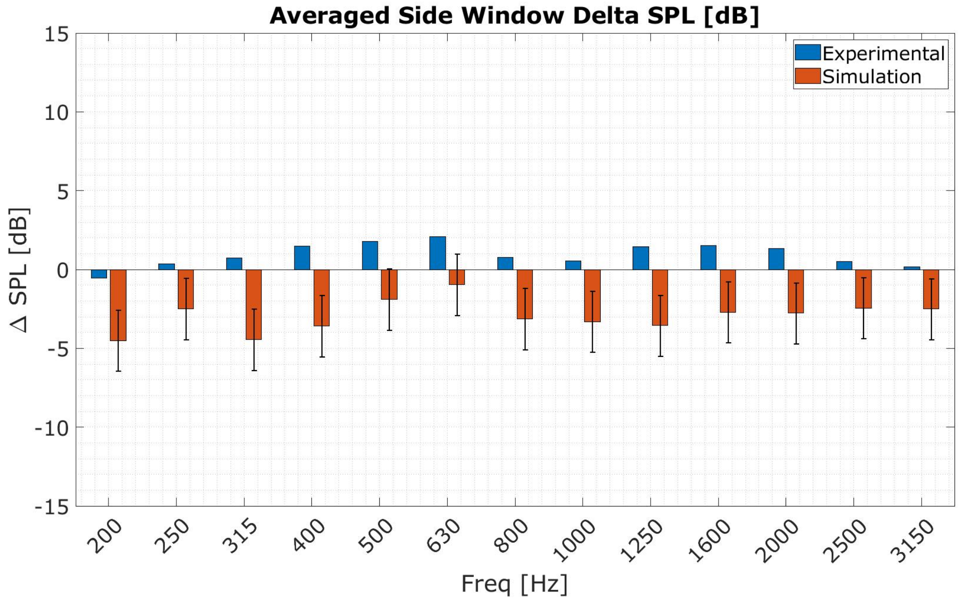

(b) Averaged delta SPL for the side window.

Figure 5.11: Experimental vs. Simulation Delta between the 20°yaw and the baseline configuration for the quarter glass 5.11a and side window 5.11b.

When comparing the simulation to the experimental data on the side window, two trends become distinguished. The experimental data predicts a positive delta on the side window as opposed to the simulation data which predicts negative deltas consistently. The quarter glass predicts a similar trend as the simulation where a increase in yaw angle decrease the sound, however, the decibel levels are noticeable in certain frequency bands. The difference between the simulation and experimental data could be due to the noise generated by the wind tunnel affecting the experimental data. As the vehicle is yawed from 10°to 20°, more influence from the noise in the wind tunnel can be observed, as seen in figure 5.11b.

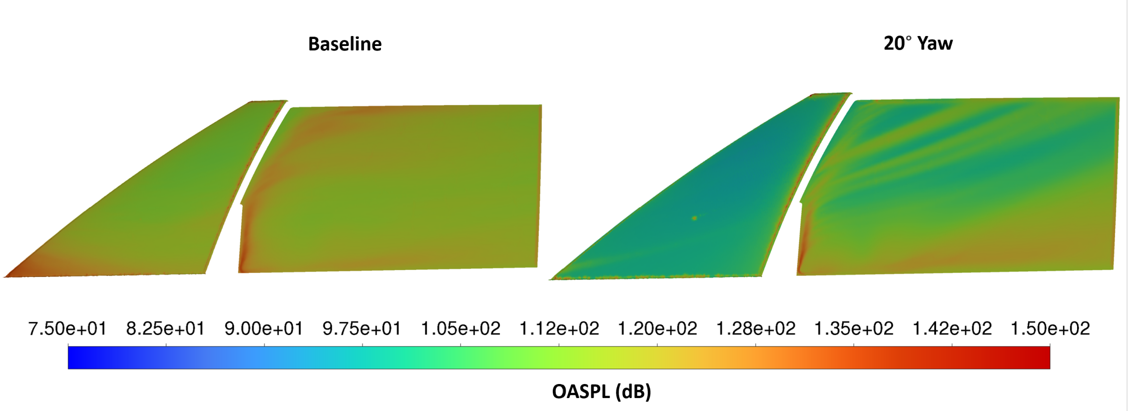

Figure 5.12: A comparison of the OASPL plots on the windows at 20°Yaw

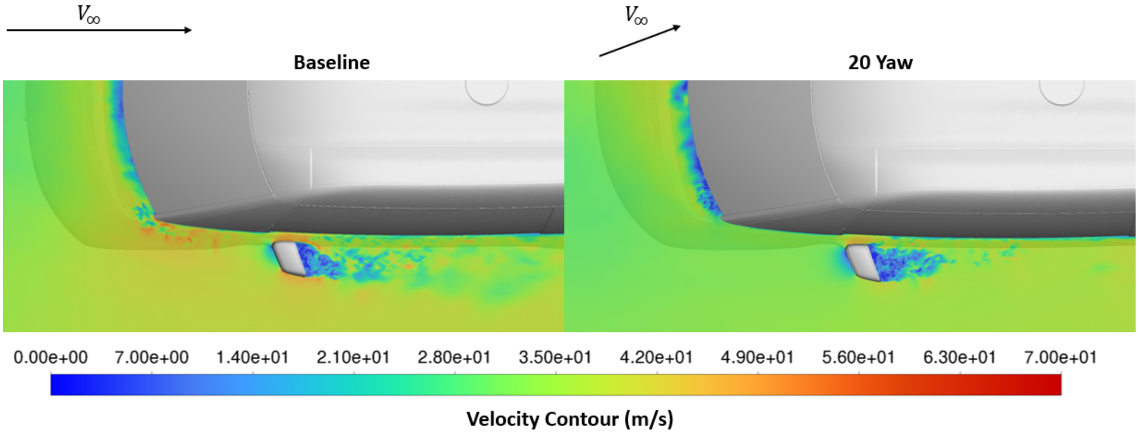

Figure 5.13: A comparison of the Velocity plots at Z = 1.37m at 20°Yaw

Figure 5.12 shows a decrease in the OASPL levels on the quarter glass and the side window. However, in the bottom right corner of the side window, an area with increased OASPL levels is noticeable. This is likely caused by the interaction between the window and the wake of the left ORVM. Figure 5.13 indicates that the wake from the left ORVM is less dominant compared to the baseline. This is because the velocity around the A-pillar region is lower than the baseline, resulting in a less intense wake.

5.1.2 Wipers Included Comparison

Another configuration is when the windshield wipers are in a lowered position as shown in figure 5.14.

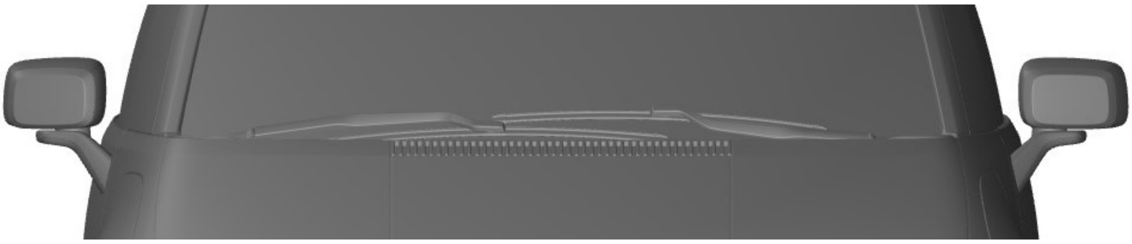

Figure 5.14: Test model with wipers.

As seen in figure 5.15, the wipers have very little affect on the SPL readings since the wipers are almost entirely enclosed by the cowl. As seen in figure 5.15a, the baseline without wipers has a higher measured SPL from 315Hz-3150Hz compared to the simulation with wipers. The same can be said for figure 5.15b for frequencies 800Hz-3150Hz. This may be the result of the windshield wipers generating a turbulent wake 5.17 interacts with the A-pillar vortex, marginally reducing it's impact on the quarter glass and side window.

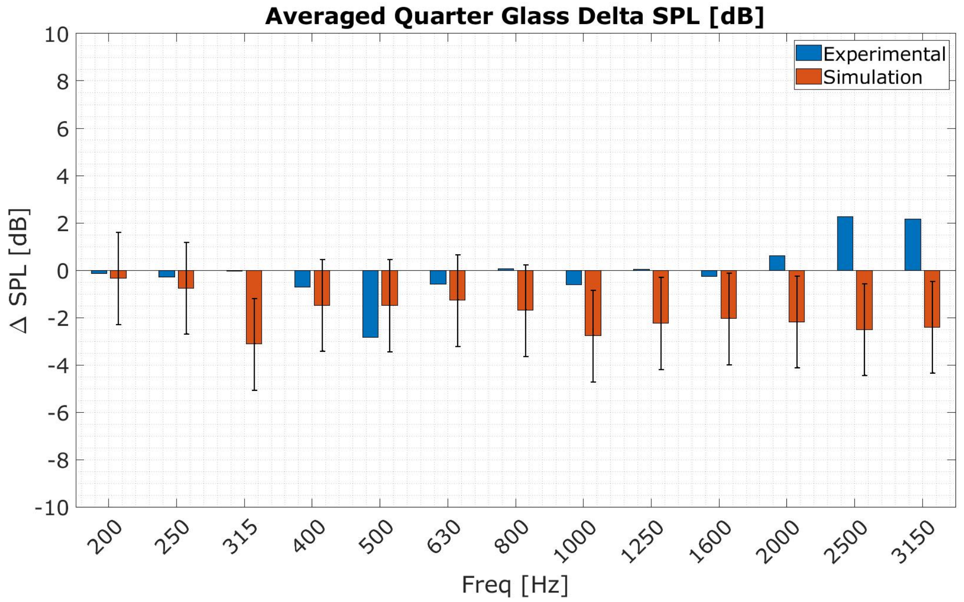

(a) Averaged Delta between the lowered wipers and baseline configurations. The measured SPL of the quarter glass is shown in decibels.

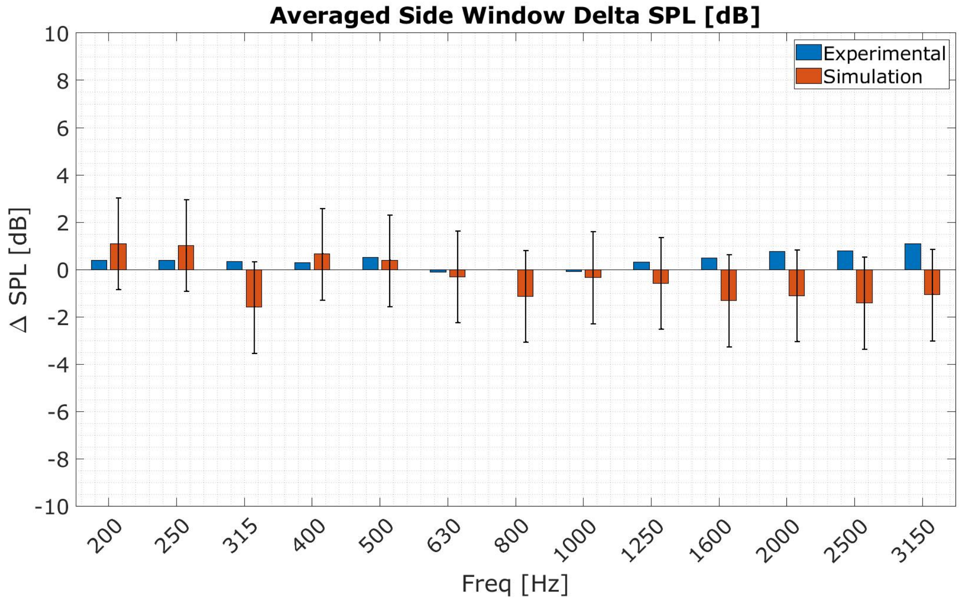

(b) Averaged Delta between the lowered wipers and baseline configurations. The measured SPL of the side window is shown in decibels.

Figure 5.15: Averaged results for the lowered wipers configuration

When looking at figure 5.17, the wipers seem to have an affect on the middle of the windscreen. This difference in flow may have affected the A-pillar vortex, as seen in Figure 5.16, where there is a slight decrease in the impact of the A-pillar vortex on the quarter glass, which can also be seen in the SPL plot in figure 5.15a.

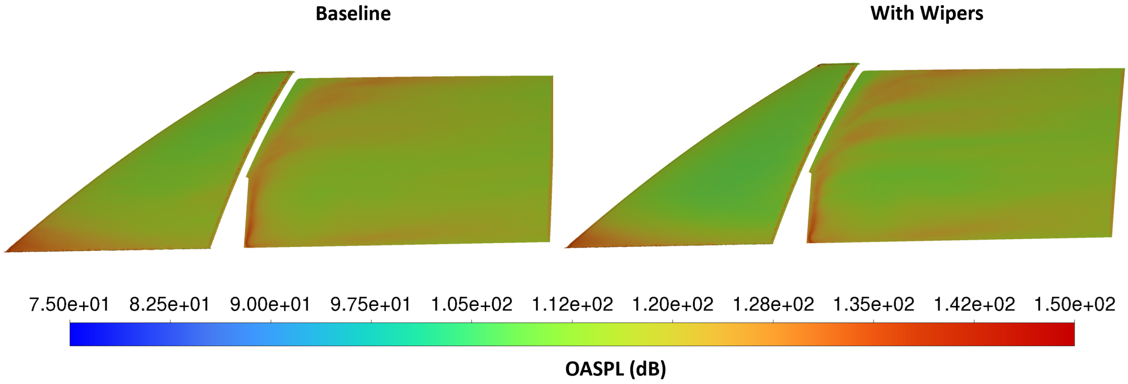

Figure 5.16: A comparison of the OASPL plots on the windows

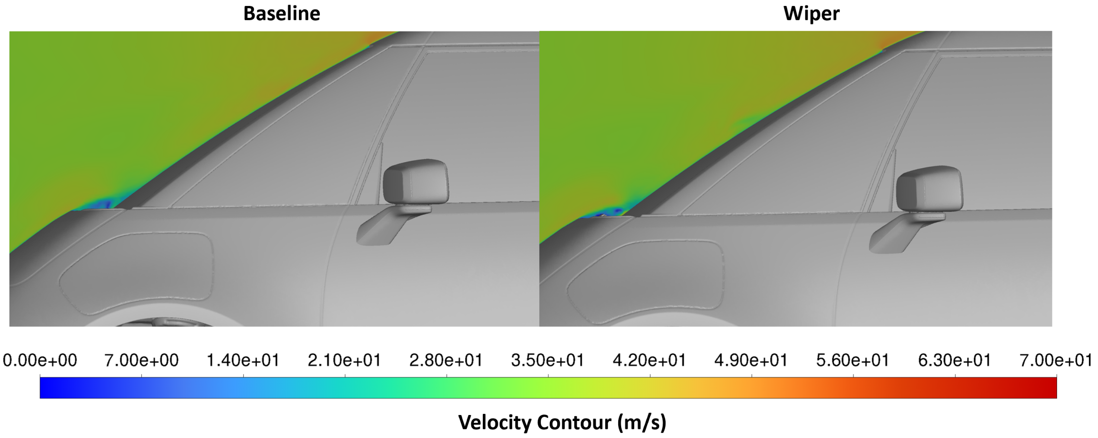

Figure 5.17: A comparison of the Velocity plots at Y = -0.6 m

5.1.3 Folded Mirror Comparison

The effect of folding the mirrors were observed to have a minimal effect on the quarter glass (see figure 5.18a) but the side window was observed to have an increase in the SPL. This increase in SPL is attributed to the turbulent wake generated by the mirrors are brought closer to the green house panels, as observed in figure 5.20. The bar graphs are also within the delta total uncertainty, further suggesting the simulation accuracy of the folded mirror geometry change.

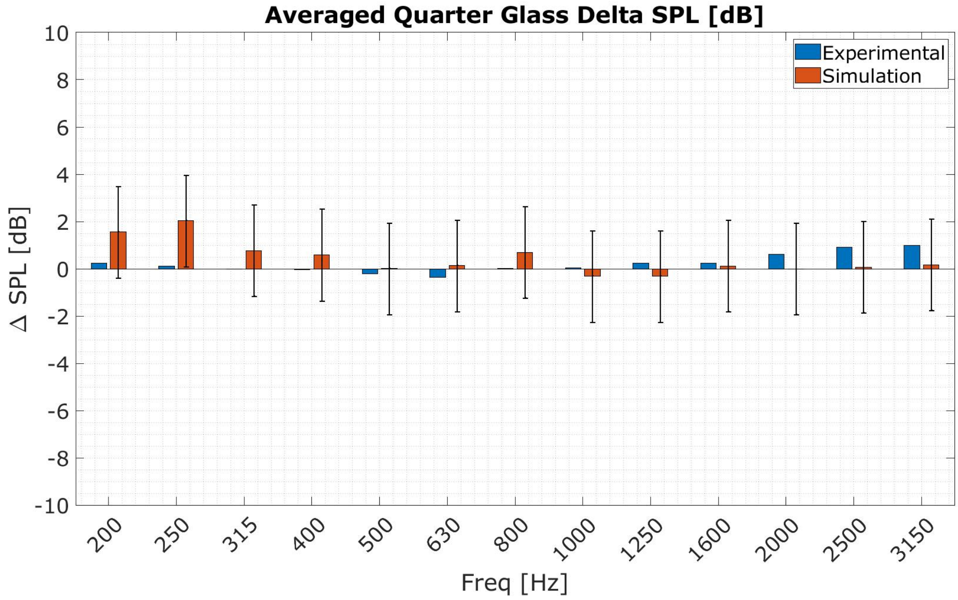

(a) Averaged Delta between the folded mirror and baseline configurations in the quarter glass.

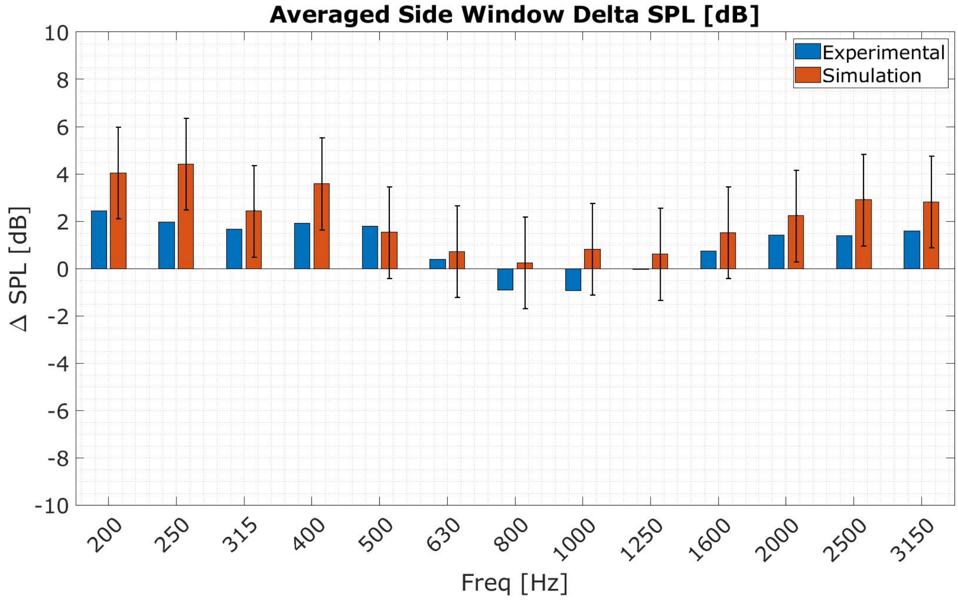

(b) Averaged Delta between the folded mirror and baseline configurations in the side window.

Figure 5.18: Delta comparison between the folded mirror and baseline configuration.

As can be observed in figure 5.20, the ORVM generates a trail of wake which interacts with the side window to produce noise. When the mirror is folded, this wake is brought closer to the window. Folding the mirror also creates a separation on the inner edge of the mirror close to the side window. This leads to a higher SPL in the lower half of the side window as displayed in figure 5.19.

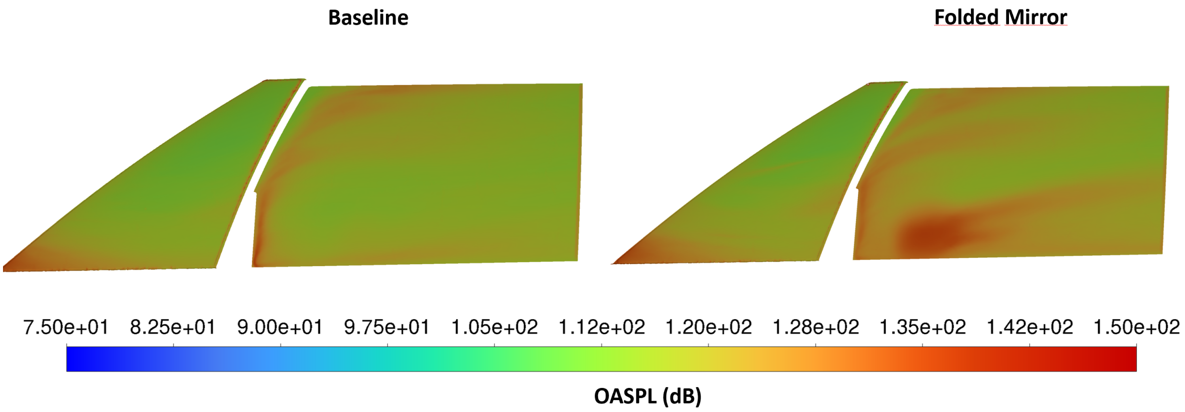

Figure 5.19: A comparison of the OASPL with the folded mirror

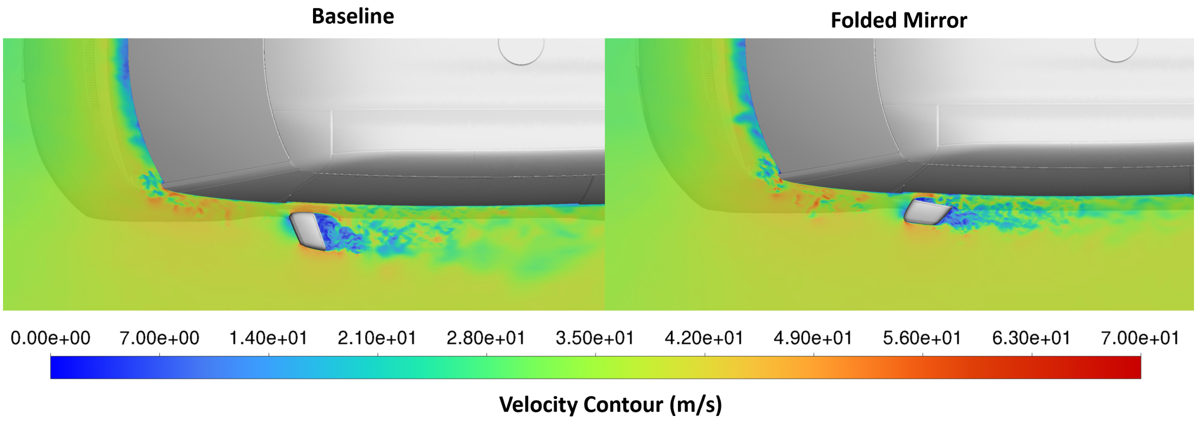

Figure 5.20: A Comparison of the wake generated by folding the mirror

5.2 ADAS Evaluation

The CFD model was shown to have good correlation with all the configurations tested in the wind tunnel. This methodology was implemented on other external geometries to evaluate their impact on the overall noise levels generated by the vehicle. The goemetry in question was the ADAS. The ADAS geometry was incorporated into the simulated geometry to see its affects on the OASPL on the vehicle. The aeroacoustic performance is analyzed using contour plots of the OASPL experienced on all exterior panels of the vehicle.

The evaluation of the ADAS system will not utilize a mesh refinement on the measured the windows of the vehicle. This had to be done to facilitate the study within the available computational resources.

Figures 5.21a and 5.21b display the ADAS baseline geometry that will be mounted as shown in figure 5.21c. The ADAS is simplified and not representative of the final ADAS that will be in place on the vehicle. The overall shape of the ADAS is not aerodynamic, suggesting that the introduction of the geometry could cause an increased in SPL on the exterior of the vehicle.

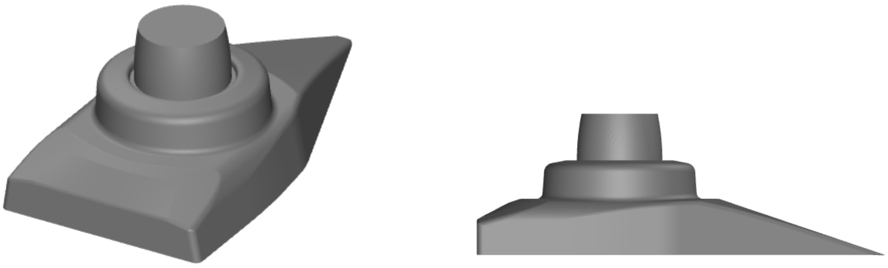

(a) Isometric view of the ADAS. **(b)** Left-hand view of the ADAS.

(c) Isometric view of the vehicle with the ADAS.

Figure 5.21: Simulated ADAS model.

5.2.1 ADAS Baseline

The ADAS baseline is as shown in figure 5.21c. The ADAS is mounted on the roof of the test object.

Upon visual inspection of figure 5.22, a clear increase in OASPL on the area surrounding the ADAS can be observed. Two particularly affected regions are infront and behind the ADAS system. Having such an increase over a large area may increase sound transmission to the front and rear seats of the vehicle through the roof panels. A small increase can also be observed at the top of the side windows, both contributing to an increase in noise transmission into the cabin.

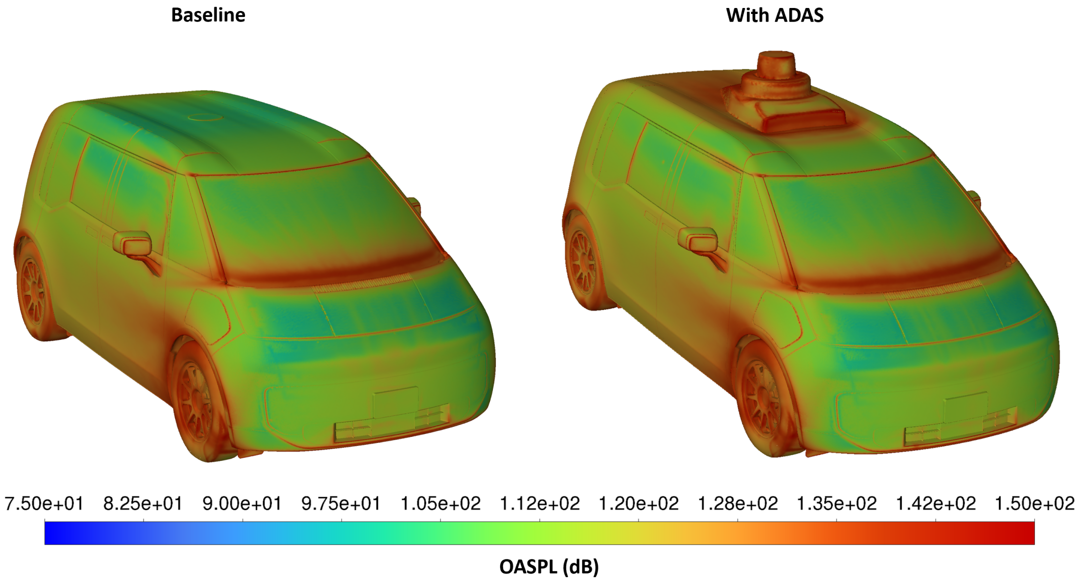

Figure 5.22: A comparison of the OASPL plots on the external body with the ADAS

Figure 5.23 shows the OASPL observed on the roof of the vehicle. An increase in OASPL can be observed around and on the ADAS. The vibrations experienced on the ADAS will transmit into the cabin. Further optimization of the ADAS geometry, particulary pertaining to the radar rings but also the blunt front geometry, needs to be investigated to mitigate sound transmission.

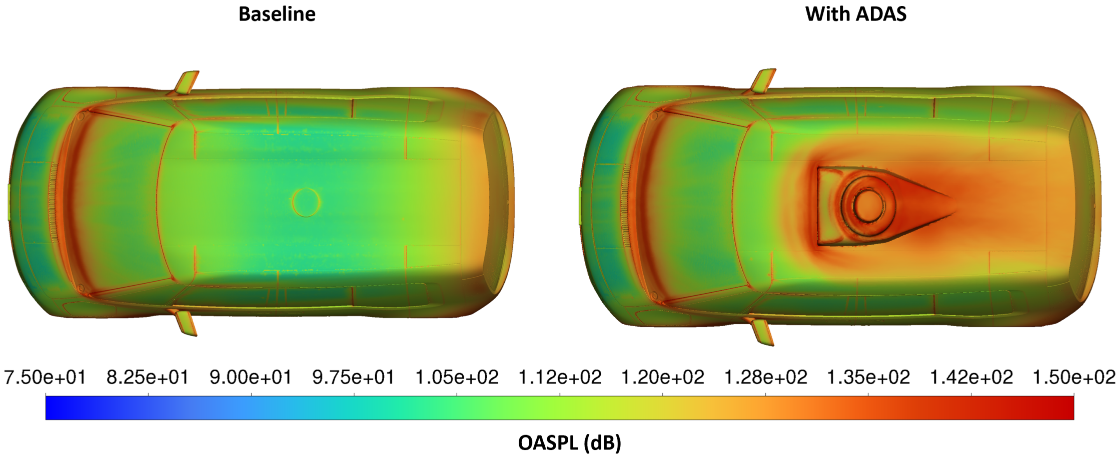

Figure 5.23: A comparison of the OASPL plots on the roof with the ADAS

5.2.2 ADAS moved forward 200mm

When observing the exterior of the vehicle, the moved ADAS seems to have a similar affect to that of the ADAS baseline. However, when the ADAS is moved forward it comes closer to the front seats of the vehicle, possibly increasing the OASPL close to the driver and passengers. It also affects more area of the roof behind the ADAS compared to the ADAS baseline, as seen in figure 5.25, potentially increasing overall noise transmission into the cabin.

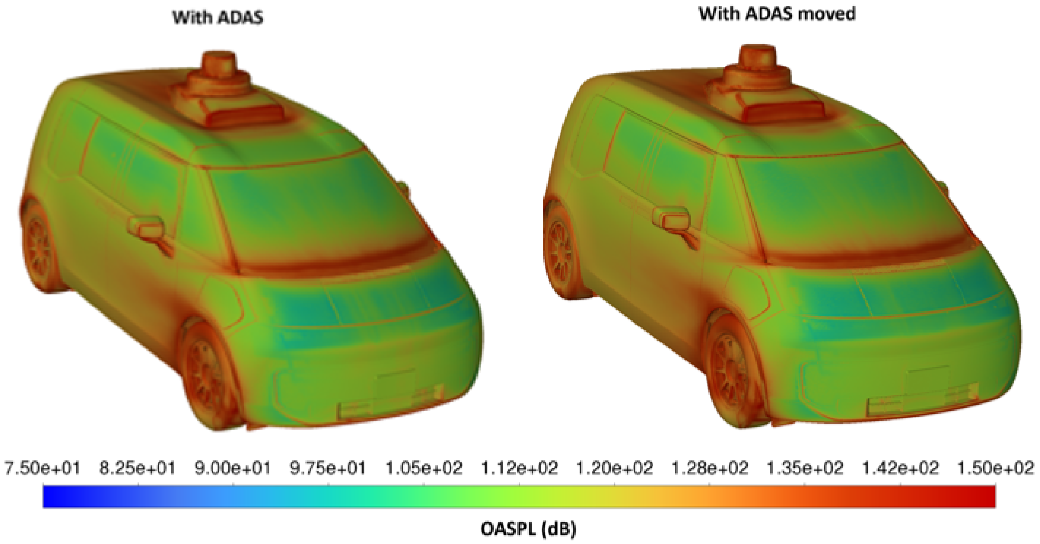

Figure 5.24: The average green house panel delta between the ADAS baseline and the moved ADAS run without refinement regions on the measured surfaces.

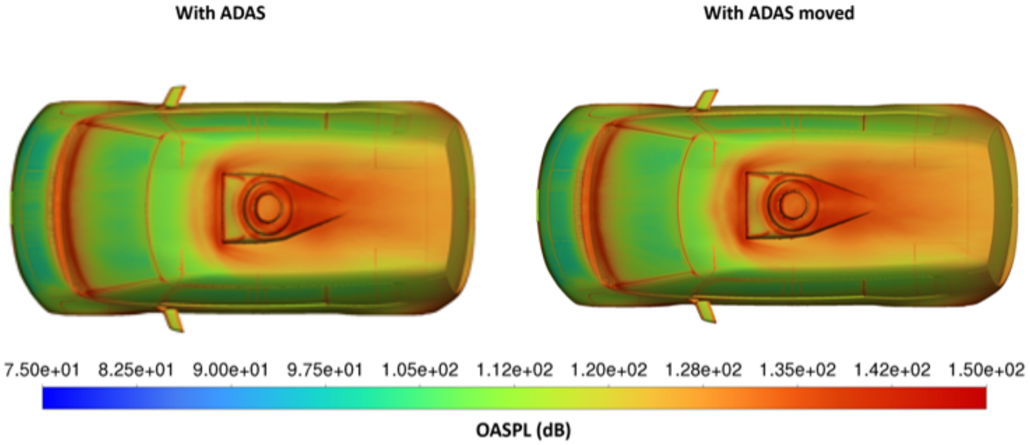

Figure 5.25: A comparison of the OASPL plots on the roof with the ADAS moved x=-200mm

6

Conclusion

In the project, a Quasi CAA method was developed to simulate the aeroacoustic noise on the external body of the vehicle. The method was verified using previous aeroacoustic wind tunnel data. This method was then implemented on certain geometry changes on the external body pertaining to the addition of new ADAS hardware to analyse the change in the noise levels on the external body.

From the mesh study, it can be concluded that a fine mesh would resolve the pressure waves adequately. This inference especially holds true for the high frequency fluctuations which would be better resolved with a finer mesh, resulting in a higher OASPL reading as observed in figure 4.16. However it was found that a 3mm refinement proved to be a sufficient trade off between the noise resolved and the computational cost. Looking at the results from the time study, it was found that running the simulation longer yielded no significant benefit to the resolved noise. A likely explaination for this is that the FFT algorithm assumes an infinitely repeating sequence of waves by applying a windowing function to make the ends of the wave have a magnitude of zero. The waves are likely to have enough data samples to produce an FFT transfrom just from 0.75s of simulation data. Hence no significant change was observed in the simulation time. The simulation time step was observed to have a significant effect on the resolved noise due to the anti-aliasing properties brought about by reducing the time step.

The results show that the Quasi CAA Method was observed to have comparable results for all simulation variations when compared with experimental data. Some simulations such as the folded mirror and -10 °yaw simulation show significant correlation to the experimental results. Due to the vast differences in setup and aeroacoustic treatment methods between the simulation and experimental test data, there is a discrepancy in the delta comparisons for the -20°yaw, 10 °yaw, 20°yaw, and lowered wiper configuration simulations. A likely reason for the discrepancy in the results for the positive yaw cases is that the accelerometers are placed in the leeward direction of the wind and hence leading to a lot of the ambient noise from the tunnel being recorded by the accelerometers. Hence a change in the nosie level due to the yaw change is not as significant as it was for the negative yaw cases. Despite these discrepancies in SPL level, the simulations mostly follow the same trend as observed in the experimental data.

While a large change in the SPL was not observed in the windows in the plots of the OASPL with the ADAS, we can see that there is a significant increase in the

OASPL level in on the roof. Sound transmission is not limited to the green house panels. Other measurement techniques, such as measuring the OASPL on the roof, may also be viable. However, it is difficult to quantify how the OASPL on the roof is transmitted through the metal and insulation into the cabin, which would require analysis of a different transmission model.

These conclusions suggest that although the absolute values may different from the wind tunnel and simulation delta comparisons, the Quasi CAA is a reliable and robust simulation method that provides results with reasonable accuracy for a large range of geometry changes on the vehicle.

7

Future Recommendations

- **Finer mesh resolution**
  For the simulations in the study, a 3mm mesh was implemented around the region of interest due to the constraints in time and resources. From the delta comparison plots with the wind tunnel data, it can be observed that in the regions of high turbulence, an overprediction in the simulation SPL values can be observed. This is presumably due to the effect of Turbulent eddies being under resolved and does not meet the recommended $l_0/\Delta x$ criterion [17]. A finer mesh around the ROI would produce a more representative delta comparison.
- **Smaller time step**
  A smaller time step was observed to mitigate the effects of aliasing and resolve the turbulent eddies better. As observed in 4.20, the resolved SPL tends to decrease in magnitude as the maximum resolved frequency (F_R) approaches Half of the sampling frequency ($F_S/2$). However reducing the time step resolves the frequency waves more accurately and for a higher SPL is observed for the same frequency bands. For future aeroacoustic simulations with more resources, the time step can be reduced further to obtain more accurate results.
- **Noise Source Region Refinement**
  For cases where the ROI is placed far from the noise source, a mesh refinement for the transmission region from the noise source to the ROI can be implemented. Currently, only a refinement region around the ROI was implemented. Having a mesh refinement for the transmission region, though would be computationally more expensive, would ensure better results in the simulations.
- **Vibro-Acoustic model for glass**
  The glass in the side window and quarter glass acts as a transmission medium. Implementing a vibro-acoustic model for the glass would allow noise to be transmitted into the cabin and could allow for a CFD model to be implemented inside the cabin to accurately simulate for the noise experienced by the passengers inside.
- **Split OASPL into frequency bands and plot on the vehicle surface**
  The human ear is more receptive to certain bands of frequency more than others. Splitting the OASPL plot data can help isolate the frequencies that the human ear is not as sensitive to. This can particularly be important if the intensity of a certain band of frequency needs to be visualized on the external surface of the vehicle, to best isolate the source of the noise.

Bibliography

[1] Perugini, C., Riccio, U., Torluccio, A., Mohr, R., et al. “An Efficient Hybrid Computational Process for Interior Noise Prediction in Aeroacoustic Vehicle Development”. In: *SAE Technical Paper Series* (2023).

[2] Council of European Union. “Council regulation (EU) no 540/2014”. 2014. URL: `http://eur-lex.europa.eu/legal-content/EN/TXT/PDF/?uri=CELEX:32014R0540&from=EN`.

[3] Mutnuri, L. R. et al. “Computational process for wind noise evaluation of rear-view mirror design in Cars”. In: *SAE Technical Paper Series* (2014). URL: `https://doi.org/10.4271/2014-01-0619`.

[4] Sebben, S. “Introduction to CFD”. 2024-03-06.

[5] L., Glegg, S. A., and Devenport, W. J. “Aeroacoustics of Low Mach Number Flows: Fundamentals, Analysis, and Measurement”. Academic Press, 2023.

[6] Berg, R. E. “Sound - Physics”. Encyclopædia Britannica, Inc. 2024-03.

[7] Patel, S. “User Guide”. Ansys Fluent. 2024-02-02.

[8] ISO. “Acoustics — Preferred reference values for acoustical and vibratory levels”. International Standard, 2015.

[9] Russelld, D. “Acoustics and Vibration Animations”. Penn State University. 2001-08.

[10] Watkins, S. “Aerodynamic noise and its refinement in vehicles”. In: (2010), pp. 219–234. DOI: `10.1533/9781845698041.3.219`. URL: `https://doi.org/10.1533/9781845698041.3.219`.

[11] Schuetz, T. “Aerodynamics of Road Vehicles, Fifth edition”. SAE international, 2016.

[12] Cochran, W., Cooley, J., Favin, D., Helms, H., Kaenel, R., Lang, W., Maling, G., Nelson, D., Rader, C., and Welch, P. “What is the fast Fourier transform?” In: *Proceedings of the IEEE* 55.10 (1967), pp. 1664–1674. DOI: `10.1109/PROC.1967.5957`.

[13] DoPA En Español. “Octaves and Third-Octaves”. `https://www.doctorproaudio.com/content.php?2402-octaves-and-third-octaves`. Accessed: 30 May 2024.

[14] Jaouen, L. “Octave and One-Third Octave Frequency Bands”. `http://apmr.matelys.com/Standards/OctaveBands.html`. Accessed: 30 May 2024. 2024.

[15] Landau, L. D. and Lifshitz, E. M. “Fluid Mechanics”. Vol. 6. U.S.S.R. Academy of Sciences, 1959.

[16] Subramaniam, S. and Balachandar, S. “Modeling Approaches and Computational Methods for Particle-Laden Turbulent Flows”. Ed. by S. Subramaniam and S. Balachandar. Academic Press, an Imprint of Elsevier, 2023.

[17] Ansys Resources. “Best Practice: RANS Turbulence Modeling in Ansys CFD | Ansys”. Accessed 16 Apr. 2024. 2024.

[18] Dempster, J. “The Laboratory Computer: A Practical Guide for Physiologists and Neuroscientists”. Academic Press, 2001.

[19] Lizhe Tan, J. J. “Digital Signal Processing (Third Edition)”. Academic Press, 2019.

[20] Chode, K. K. et al. “Investigating the aerodynamic drag and noise characteristics of a standard squareback vehicle with inclined side-view mirror configurations using a hybrid computational aeroacoustics (CAA) approach”. In: *Physics of Fluids* 35.7 (2023-07). DOI: `10.1063/5.0156111`. URL: `https://doi.org/10.1063/5.0156111`.

[21] Stridh, M. “Joint Optimization of Aerodynamics and Aeroacoustics of Side View Mirrors”. 2018.

[22] He, Y. et al. “Wind noise source filtering and transmission study through a side glass of DrivAer model”. In: *Applied Acoustics* 160 (2020-03), p. 107161. DOI: `10.1016/j.apacoust.2019.107161`. URL: `https://doi.org/10.1016/j.apacoust.2019.107161`.

[23] He, Y., Schröder, S., Shi, Z., Blumrich, R., Yang, Z., and Wiedemann, J. “Wind noise source filtering and transmission study through a side glass of DrivAer model”. In: *Elsevier Ltd* (2019).

[24] Roditcheva, O., Lofdahl, L., Sebben, S., Harling cEng, P., et al. “On the Possibilities and Limitations of Wind Noise Testing in the Aerodynamical Wind Tunnel at Volvo Cars”. In: *SAE Technical Paper Series* (2016).

[25] Ansys Fluent Aeroacoustics. “Lecture 02: Computational Aeroacoustics (CAA)”. Accessed 16 Apr. 2024. 2023.

[26] Caldwell, J. and Vahidsafa, A. “Propagation of Error”. `https://chem.libretexts.org/Bookshelves/Analytical_Chemistry/Supplemental_Modules_(Analytical_Chemistry)/Quantifying_Nature/Significant_Digits/Propagation_of_Error`. Accessed: 2023-08-29. 2023.

[27] Rider, G. “Encyclopedia of Toxicology (Second Edition)”. Elsevier, 2005.

DEPARTMENT OF SOME SUBJECT OR TECHNOLOGY
CHALMERS UNIVERSITY OF TECHNOLOGY
Gothenburg, Sweden
www.chalmers.se

CHALMERS
UNIVERSITY OF TECHNOLOGY